Research Article

Journal of Environmental Nanotechnology

Sustainable MnO_2/Biochar Nanocomposite from Pomegranate Peel for Rhodamine B Removal: Statistical Optimization and Machine Learning

S. ShivaPrakash[1], Suvetha Poyyamani Sunddararaj[2*], S. Rakesh[3], M. Bala Prabhakar[4], Syed Inthiyaz[5] and Dhanasekaran Arumugam[6]

[1]Department of Mechanical Engineering, New Horizon College of Engineering, Bengaluru, KA, India
[2]Department of Electrical and Electronics Engineering, Dayananda Sagar College of Engineering, Bengaluru, KA, India
[3]Department of Mechanical Engineering, Francis Xavier Engineering College, Tirunelveli, TN, India
[4]Department of Mathematics, Aditya University, Surampalem, AP, India
[5]Department of Electronics and Communication Engineering, Koneru Lakshmaiah Education Foundation, Guntur, AP, India
[6]Department of Mechanical Engineering, Academy of Maritime Education and Training (AMET), Deemed to be University, Kanathur, Chennai, TN, India

Received: 29.07.2026 Accepted: 28.08.2026 Published: xx.xx.xxxx

*suvethaps16@gmail.com

ABSTRACT

This study developed an MnO_2/biochar nanocomposite derived from pomegranate peel and investigated its performance for removing Rhodamine B from aqueous media. The prepared adsorbent was characterized using FTIR, BET, UV–Vis, PXRD, and FESEM analyses to determine its functional groups, porous characteristics, optical behaviour, crystalline phases, and surface morphology. A Taguchi L27 design, signal-to-noise analysis, and ANOVA were employed to examine the effects of contact time, adsorbent dosage, solution pH, and initial dye concentration. MEREC weighting and MABAC ranking were subsequently integrated for simultaneous optimization of removal efficiency and adsorption capacity. Taguchi analysis predicted the preferred factor-level combination as 60 min, pH 10, 0.05 g dosage, and 75 mg L^{-1} concentration, whereas MABAC identified Run 24 (60 min, pH 7, 0.05 g, and 75 mg L^{-1}) as the best condition among the experimentally tested L27 alternatives, yielding 74.50% removal and 85.53 mg g^{-1} adsorption capacity. The engineered-input ANN–GA models produced cross-validated R^2 values of 0.8488 and 0.9173 for removal efficiency and adsorption capacity, respectively. However, quadratic regression achieved higher leave-one-out R^2 values of 0.9265 and 0.9777, indicating better generalization than ANN–GA for the limited L27 dataset. The proposed framework demonstrates the combined application of statistical design, objective weighting, multi-criteria ranking, and machine learning for evaluating Rhodamine B adsorption by the MnO_2/biochar nanocomposite.

Keywords: Nanocomposite; Rhodamine B; Adsorbent dosage; ANOVA; Adsorption.

1. INTRODUCTION

Agricultural waste-derived adsorbents have gained considerable attention as sustainable and low-cost materials for wastewater treatment. Activated carbon prepared from teff grass straw was investigated for the removal of Pb (II) ions from wastewater, demonstrating effective heavy metal remediation using agro-waste-derived activated carbon (Sugumar *et al.* 2024). Modified biocarbon prepared from teff hay was subsequently evaluated for cadmium removal from electroplating wastewater, confirming its applicability as an efficient and sustainable adsorbent for industrial treatment (Rao *et al.* 2025). Green carbon fibers produced from banana pseudostem exhibited excellent adsorption performance toward lead ions, highlighting the potential of agricultural residues as eco-friendly adsorbents (Kumar *et al.* 2026). Green-synthesized nanoparticles prepared from moringa seed waste, pomegranate peel, and sawdust achieved efficient Cr (VI) removal, with pomegranate peel-based nanomaterials exhibiting continuous-flow removal efficiencies of 96–100% and a maximum adsorption capacity of 88.22 mg g^{-1} (Mahdy and Fathi, 2026). Rhodamine B (RhB) is a persistent synthetic dye commonly present in industrial effluents, and its removal using semiconductor-based photocatalysis has received considerable attention (Loganathan *et al.* 2026).

Pomegranate peel has emerged as a promising biomass precursor for developing high-performance adsorbents and photocatalysts because of its abundant functional groups and carbon-rich composition. Raw pomegranate peel effectively removed Brilliant Blue R and Victoria Blue R dyes with removal efficiencies of 90.38% and 100%, respectively (Akmese, 2025). Microwave-assisted activated carbon synthesized from pomegranate peel waste achieved a maximum Congo Red adsorption capacity of 26.93 mg g^{-1} (Benahdach *et*

al. 2025). A kaolinite-modified pomegranate hydrochar composite exhibited a maximum malachite green adsorption capacity of 28.20 mg g^{-1} (Azizi and Alorabi, 2025). Raw pomegranate peel-loaded ZIF-8 demonstrated 99.18% Rhodamine B removal with a maximum adsorption capacity of 782 mg g^{-1} and excellent regeneration performance (Kamalesh and Saravanan, 2026). A cellulose/chitosan composite prepared from pomegranate peel achieved more than 95% methyl orange removal while exhibiting excellent stability and reusability (Fadhil *et al.* 2026). An $AgFeO_2$/pomegranate peel activated carbon nanocomposite exhibited adsorption capacities of 798.6 mg g^{-1} for Neutral Red and 598 mg g^{-1} for Brilliant Blue R under visible-light irradiation (El-Mahdy *et al.* 2026). A green SnO_2–TiO_2 nanocomposite synthesized using pomegranate peel extract achieved 97.56% photocatalytic degradation of Alizarin Red dye within 100 min (Sumathi *et al.* 2026). Similarly, a green-mechanochemically synthesized $NiFe_2O_4$@rGO hybrid achieved more than 99% degradation of RhB within 60 min under UV irradiation because of improved electron transport and active-site utilization (Ganvir *et al.* 2026).

MnO_2-based photocatalysts have also demonstrated remarkable potential for wastewater remediation because of their superior catalytic activity and visible-light responsiveness. A hierarchical MnO_2@ZIF-8 core–shell photocatalyst achieved more than 96% Rhodamine B degradation through a Fenton-like process (Cao *et al.* 2022). An α-MnO_2/GO/PVDF catalytic membrane simultaneously separated and degraded dyes while maintaining excellent reusability (He *et al.* 2026). A SiNWs/MnO_2/$Ni(OH)_2$ heterostructure achieved 93% Rhodamine B degradation under visible-light irradiation (Derkaoui *et al.* 2025). An iodine-doped MnO_2/polythiophene nanocomposite removed 95% of Rhodamine B within 90 min (Nayab *et al.* 2026). A TiO_2/MnO_2-coated reactive ceramic membrane integrated with catalytic ozonation achieved complete Rhodamine B degradation within 40 min (Chen *et al.* 2023). A reusable MnO_2 nanosheet-coated nickel foam catalyst removed more than 92% of Rhodamine B within 60 min while maintaining excellent cycling stability (Li *et al.* 2026). A hydrothermally synthesized MWCNT/Ag/β-MnO_2 hybrid photocatalyst achieved 87% degradation of mixed dye solutions under visible light (Kreetachat *et al.* 2026). A microwave-assisted MnO_2/rGO nanocomposite exhibited superior photocatalytic performance and enhanced stability compared with pristine MnO_2 (Kandasamy *et al.* 2026).

Optimization approaches based on statistical and artificial intelligence techniques have further improved wastewater treatment processes. Response surface methodology coupled with artificial neural networks and genetic algorithms identified optimum microwave-assisted extraction conditions of 685 W, 75 °C, and 24 min (More and Arya, 2024). Central composite design combined with response surface methodology and ANOVA successfully optimized crystal violet adsorption using raw and $SnCl_2$/$FeCl_2$-modified pomegranate peel, achieving maximum adsorption capacities of 172.40 and 389.88 mg g^{-1}, respectively (Hamrouche *et al.* 2025). Ce-doped TiO_2 nanoparticles also achieved approximately 98% UV-assisted degradation of RhB, which was attributed to band-gap reduction, enhanced light absorption, and effective charge-carrier separation (Deepha and Senthilnathan, 2026).

Despite numerous studies on Rhodamine B removal, the combined optimization of removal efficiency and adsorption capacity using pomegranate-peel-derived MnO_2/biochar remains insufficiently investigated. Previous studies have generally applied statistical optimization, multi-criteria decision-making, or machine learning separately. The novelty of this study lies in integrating Taguchi–ANOVA for factor screening, MEREC for objective response weighting, MABAC for ranking experimentally tested alternatives, and ANN–GA for nonlinear prediction. This unified framework distinguishes the statistically predicted factor-level combination from the best experimentally tested multi-response condition while comprehensively evaluating the adsorption behaviour of the nanocomposite.

2. MATERIALS AND METHODOLOGY

2.1 Materials

Pomegranate peels were collected as the biochar precursor. Rhodamine B, potassium permanganate, manganese sulfate, ethanol, hydrochloric acid and sodium hydroxide were obtained from Sigma-Aldrich. Deionized water was used for nanocomposite preparation, solution dilution and adsorption experiments.

2.2 Preparation of Rhodamine B Solutions

A Rhodamine B stock solution with a concentration of 100 mg L^{-1} was prepared by dissolving 0.1 g of dye in 1000 mL of deionized water. The solution was stirred until complete dissolution and subsequently transferred to an amber glass container to minimize light-induced degradation. Working solutions containing 25, 50 and 75 mg L^{-1} Rhodamine B were prepared from the stock solution by serial dilution with deionized water. The required solution pH values of 4, 7 and 10 were adjusted using dilute hydrochloric acid or sodium hydroxide before the adsorption experiments.

2.3 Preparation of Pomegranate-peel Biochar

Fresh pomegranate peels were thoroughly washed with tap water followed by deionized water to remove adhering impurities. The cleaned peels were cut

into small pieces, oven-dried at 60 °C for 24 h, ground and passed through a 250 µm sieve. Chemical activation was performed by mixing the peel powder with potassium hydroxide at a precursor-to-KOH mass ratio of 1:2. The mixture was dispersed in deionized water and continuously stirred for 3 h to facilitate impregnation. It was then dried and pyrolysed at 500 °C for 2 h in a nitrogen atmosphere using a heating rate of 10 °C min^{-1}. After cooling, the resulting biochar was washed with dilute hydrochloric acid and deionized water until a neutral filtrate was obtained. The prepared pomegranate-peel biochar was subsequently dried at 80 °C, ground, and stored in an airtight container. Likewise, pomegranate-peel biochar was produced by washing, drying, grinding, and pyrolyzing the peels under oxygen-limited conditions for wastewater adsorption (Murat *et al.* 2025).

2.4 Synthesis of the MnO_2/Biochar Nanocomposite

The MnO_2/biochar nanocomposite was produced through an in-situ redox precipitation process. Pomegranate-peel biochar (5 g) was dispersed in 100 mL of 0.05 mol L^{-1} potassium permanganate solution and ultrasonicated for 30 min to obtain a uniform suspension. A 0.10 mol L^{-1} manganese sulfate solution was added dropwise under continuous stirring. The reaction mixture was maintained at 60 °C for 4 h to promote the nucleation and deposition of MnO_2 particles over the biochar surface. Similarly, MnO_2 nanoparticles were green-synthesized using pomegranate-peel extract as a reducing and stabilizing agent, followed by drying and calcination (Aslam *et al.* 2025). The formed composite were separated by filtration, repeatedly washed with deionized water and ethanol, and dried at 80 °C for 12 h. The dried material was gently ground, sieved, and stored in a sealed container for characterization and Rhodamine B adsorption experiments.

$$2MnO_4^- + 3Mn^{2+} + 2H_2O \rightarrow 5MnO_2 + 4H^+ \quad \ldots (1)$$

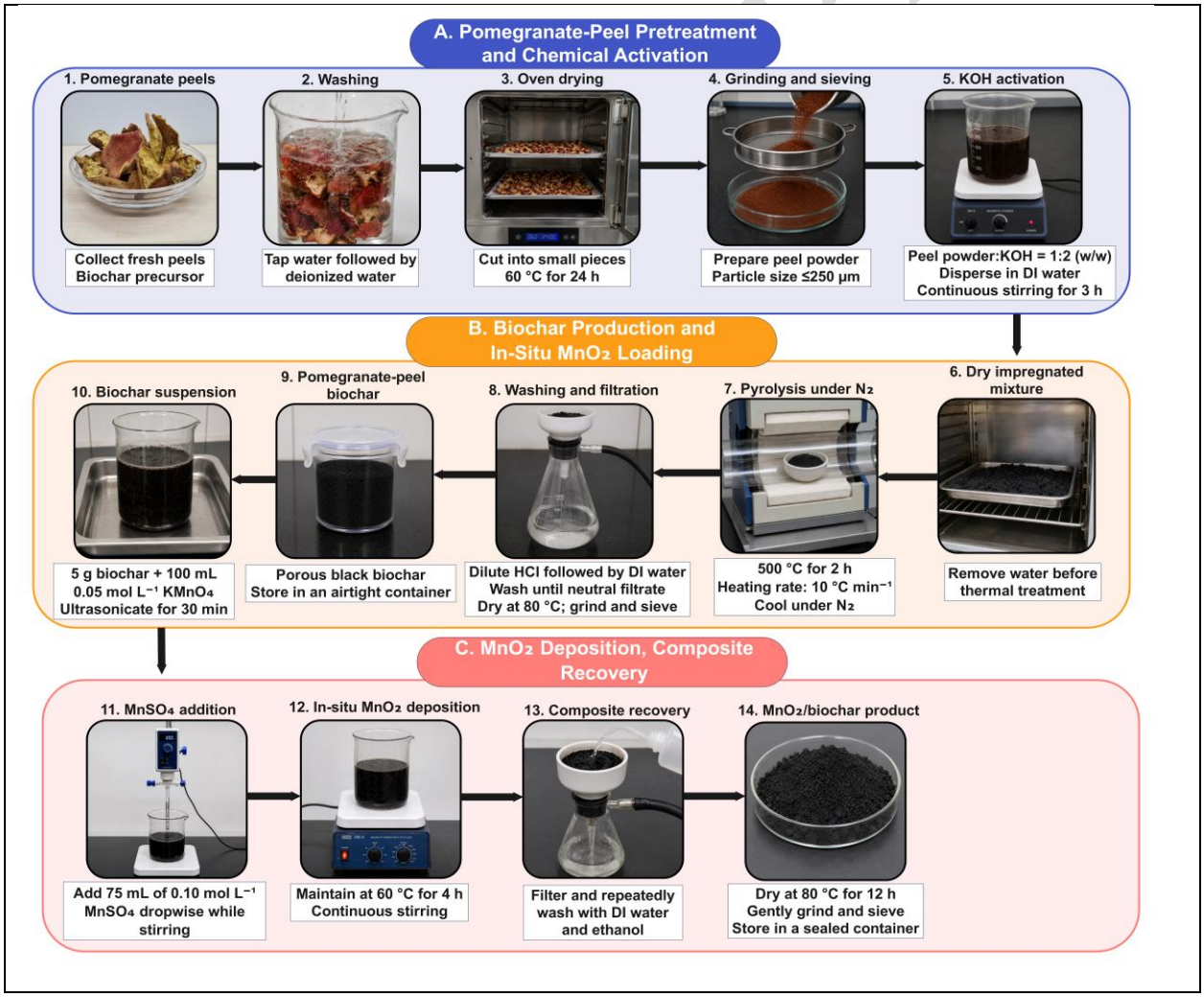

Fig. 1: Preparation of the MnO_2/biochar nanocomposite

2.5 Characterization of the MnO_2/Biochar Nanocomposite

The physicochemical characteristics of the prepared MnO_2/biochar nanocomposite were examined using Fourier-transform infrared spectroscopy, ultraviolet–visible spectroscopy (UV–Vis), field-emission scanning electron microscopy coupled with energy-dispersive X-ray spectroscopy (FESEM–EDX), powder X-ray diffraction (PXRD), and Brunauer–Emmett–Teller (BET) surface-area analysis. These techniques were used to determine the surface functional groups, optical absorption behaviour, morphology, elemental composition, crystalline phases, specific surface area and pore characteristics of the adsorbent.

2.5.1 Fourier-transform Infrared Spectroscopy

The functional groups present on pomegranate-peel biochar and the MnO_2/biochar nanocomposite were identified using an FTIR spectrometer (Bruker Vertex 70). Spectra were recorded over the wavenumber range of 4000–400 cm^{-1}. The observed changes in the position and intensity of hydroxyl, carbonyl, aromatic and metal–oxygen bands were examined to verify MnO_2 deposition and identify the functional groups potentially involved in Rhodamine B adsorption.

2.5.2 Ultraviolet−visible Spectroscopy

Optical absorption properties of prepared materials were investigated using UV–Vis spectroscopy. Approximately 0.5 mg mL^{-1} of each sample was dispersed in deionized water or ethanol and ultrasonicated for 30 min to obtain a uniform suspension. Absorption spectra was recorded between 200 and 800 nm using an appropriate solvent as the reference. The absorption features associated with the carbonaceous structure and manganese oxide were evaluated to examine the optical behaviour of the nanocomposite.

2.5.3 Field-emission Scanning Electron Microscopy and Elemental Analysis

Surface morphology of pomegranate-peel biochar and MnO_2/biochar nanocomposite was examined using a GeminiSEM 500 field-emission scanning electron microscope. Before imaging, the dried samples were mounted on conductive carbon tape and coated with a thin conductive layer when necessary. Images obtained at various magnifications were used to assess surface roughness, pore formation, particle distribution and MnO_2 agglomeration. Energy-dispersive X-ray spectroscopy were additionally employed to verify presence and distribution of carbon, oxygen and manganese within the nanocomposite.

2.5.4 Powder X-ray Diffraction Analysis

PXRD patterns were recorded using Cu Kα radiation (λ = 1.5406 Å) over a 2θ range of 10–80°, with a step size of 0.02° and a scanning rate of 2° min^{-1}. The instrument was operated at 40 kV and 30 mA. The resulting peaks were compared with standard crystallographic data to confirm the characteristic phases of MnO_2. The broad carbon reflection was examined to evaluate the amorphous or partially graphitic structure of the pomegranate-peel biochar.

2.5.5 Brunauer-Emmett-Teller Analysis

Specific surface area, pore-size distribution and pore volume of MnO_2 /biochar nanocomposite was determined from nitrogen adsorption-desorption measurements by Gemini Micromeritics surface-area analyser. Before BET analysis, approximately 0.20 g of the MnO_2/biochar nanocomposite was degassed under vacuum at 150 °C for 6 h to remove adsorbed moisture and volatile impurities. Nitrogen adsorption–desorption measurements were subsequently performed at 77 K. The specific surface area was determined using the BET method, while the pore-size distribution and total pore volume were evaluated using the BJH method. The BET surface area was calculated using:

$$\frac{P/P^0}{V_{\text{ads}}(1-P/P^0)} = \frac{1}{CV_{\text{m}}} + \frac{C-1}{CV_{\text{m}}}\left(\frac{P}{P^0}\right) \quad \ldots (2)$$

P represents equilibrium pressure, P^0 were saturation vapour pressure, V_{ads} denotes volume of adsorbed nitrogen, V_{m} is the monolayer adsorption capacity and C were the BET constant associated with adsorption energy.

2.6 Rhodamine B Adsorption Experiments

Batch experiments were conducted to evaluate Rhodamine B adsorption by the MnO_2 /biochar nanocomposite. The experimental variables were contact time of 20, 40 and 60 min; solution pH of 4, 7 and 10; adsorbent dosage of 0.05, 0.10 and 0.15 g; and initial dye concentration of 25,50 and $75 mgL^{-1}$. The pH was adjusted by dilute HCl or NaOH. Each suspension was agitated at 180 rpm and 25°C for the contact period specified by the Taguchi L27 design.

After adsorption, the nanocomposite was separated through centrifugation, and residual dye concentration at supernatant were measured by UV-Vis spectrophotometer at the experimentally determined Rhodamine B maximum absorption wavelength, approximately 554 nm. Removal efficiency was calculated using eqn (3):

$$R(\%) = \frac{C_0 - C_e}{C_0} \times 100 \quad \ldots (3)$$

where R is the removal efficiency, C_0 were initial dye concentration and C_e were final Rhodamine B concentration in mgL^{-1}.

Equilibrium adsorption capacity were determined by:

$$q_e = \frac{(C_0 - C_e)V}{m} \quad \ldots (4)$$

where q_e were adsorption capacity in mgg^{-1}, V were solution volume in litres and m were mass of MnO_2 biochar nanocomposite in grams. All experiments were performed in triplicate, and the results were expressed as mean ± standard deviation.

2.7 Taguchi L27 Experimental Design

Taguchi L27 orthogonal array were employed to investigate effects of contact time, solution pH, MnO_2 /biochar dosage and initial Rhodamine B concentration at removal efficiency and adsorption capacity. Batch adsorption experiments were performed using 50 mL of Rhodamine B solution in 100 mL Erlenmeyer flasks at 25 ± 2 °C. The suspensions were agitated at 150 rpm using an orbital shaker for the specified contact times of 20, 40, and 60 min. Following adsorption, the suspensions were centrifuged at 6000 rpm for 10 min to separate the adsorbent. The residual Rhodamine B concentration in the supernatant was determined using a UV–Vis spectrophotometer at its maximum absorption wavelength of 554 nm. All experiments were performed in triplicate, and the results were reported as mean ± standard deviation. Each factor was examined at three levels, resulting in 27 experimental combinations. Selected control factors and their levels were presented in Table 1. To ensure experimental reproducibility, identical operating and analytical conditions were maintained throughout the adsorption experiments. Each Taguchi L27 condition was independently evaluated in triplicate using a fixed solution volume of 50 mL at 25 ± 2 °C and an agitation speed of 150 rpm. After the specified contact time, the suspensions were centrifuged at 6000 rpm for 10 min, and the residual Rhodamine B concentration was determined at 554 nm. The same solution preparation, pH adjustment, adsorption, separation and analytical procedures were followed for all experimental runs and confirmation tests. The measured responses were expressed as mean ± standard deviation to account for experimental variability and improve the reliability of the reported results.

Table 1. Control factors and levels used in the Taguchi L27 design

Factor	Symbol	Level 1	Level 2	Level 3
Contact time	A	20	40	60
Solution pH	B	4	7	10
MnO_2 /biochar	C	0.05	0.10	0.15
Initial Rhodamine B concentration	D	25	50	75

Because higher removal efficiency and adsorption capacity were preferred, larger-the-better signal-tonoise ratio were calculated using:

$$\frac{S}{N} = -10\log_{10}\left[\frac{1}{n}\sum_{i=1}^{n}\frac{1}{y_i^2}\right] \quad \ldots (5)$$

where n were number of replicate measurements and y_i is the measured response. The mean response and S/N ratio at each factor level were used to determine the main effects. Factors were ranked according to their delta values, calculated as the difference between the highest and lowest level averages:

$$\Delta_j = \max(\bar{y}_{j1}, \bar{y}_{j2}, \bar{y}_{j3}) - \min(\bar{y}_{j1}, \bar{y}_{j2}, \bar{y}_{j3}) \quad \ldots (6)$$

where Δ_j is the response range of factor j, and $\bar{y}_{jk}$ is the average response of factor j at level k. Level associated with highest larger-the-better S/N ratio was selected as the preferred level for each factor.

2.8 Analysis of Variance

Analysis of variance was independently performed for removal efficiency and adsorption capacity to determine the statistical importance of the four adsorption variables. The total response variation was partitioned into the contributions of contact time, solution pH, MnO_2 /biochar dosage, initial Rhodamine B concentration and experimental error.

Mean square for each factor was calculated as:

$$MS_j = \frac{SS_j}{DF_j} \quad \ldots (7)$$

where MS_j, SS_j and DF_j are the mean square, sum of squares and degrees of freedom of factor j, respectively. The F-value was determined from:

$$F_j = \frac{MS_j}{MS_e} \quad \ldots (8)$$

where MS_e is the residual mean square. The percentage contribution of each factor was calculated using:

$$P_j(\%) = \frac{SS_j}{SS_T} \times 100 \quad \ldots (9)$$

where SS_T represents the total sum of squares. A factor was considered statistically significant when its

probability value was below 0.05 at the 95% confidence level.

2.9 MEREC Objective Weighting

Method based on the Removal Effects of Criteria were applied to determine objective weights for removal efficiency and adsorption capacity. The 27 Taguchi runs were considered alternatives, while the two measured responses were treated as beneficial criteria.

For MEREC calculation, each beneficial response was normalized using:

$$n_{ij} = \frac{\min_i(x_{ij})}{x_{ij}} \quad \ldots (10)$$

where x_{ij} is the performance of run i under criterion j, and n_{ij} is its normalized value. The overall performance of each experimental run was calculated from:

$$S_i = \ln\left[1 + \frac{1}{m}\sum_{j=1}^{m} \left|\ln\left(n_{ij}\right)\right|\right] \quad \ldots (11)$$

where m denotes the number of response criteria. The performance after removing criterion j was determined using:

$$S'_{ij} = \ln\left[1 + \frac{1}{m}\sum_{\substack{k=1 \\ k\neq j}}^{m} \left|\ln\left(n_{ik}\right)\right|\right] \quad \ldots (12)$$

The removal effect of each criterion was subsequently obtained from:

$$E_j = \sum_{i=1}^{N} \left|S'_{ij} - S_i\right| \quad \ldots (13)$$

where N is the number of experimental runs. The final MEREC weight was calculated as:

$$w_j = \frac{E_j}{\sum_{k=1}^{m} E_k} \quad \ldots (14)$$

where w_j represents the objective weight of criterion j, and the sum of all criterion weights equals one.

2.10 MABAC Multi-response Ranking

The Multi-Attributive Border Approximation Area Comparison method was integrated with the MEREC weights to rank the 27 experimental conditions. Removal efficiency and adsorption capacity were treated as beneficial criteria and normalized through:

$$r_{ij} = \frac{x_{ij} - \min_i(x_{ij})}{\max_i(x_{ij}) - \min_i(x_{ij})} \quad \ldots (15)$$

The weighted normalized decision matrix was obtained from:

$$v_{ij} = w_j\left(r_{ij} + 1\right) \quad \ldots (16)$$

where v_{ij} is the weighted performance and w_j is the MEREC weight. The border approximation value for each criterion was calculated using the geometric mean:

$$g_j = \left(\prod_{i=1}^{N} v_{ij}\right)^{1/N} \quad \ldots (17)$$

The distance of each alternative from the border approximation area was determined using:

$$q_{ij} = v_{ij} - g_j \quad \ldots (18)$$

A positive distance indicates that the experimental condition belongs to the upper approximation area, whereas a negative value indicates the lower approximation area. The final MABAC score was calculated as:

$$Q_i = \sum_{j=1}^{m} q_{ij} \quad \ldots (19)$$

The experimental runs were arranged in descending order of Q_i, and the condition with the highest score were selected as best experimentally tested compromise between removal efficiency and adsorption capacity.

2.11 ANN-GA Modelling

An artificial neural network integrated with a genetic algorithm was developed in MATLAB to model removal efficiency and adsorption capacity. Contact time, solution pH, MnO_2 /biochar dosage and initial Rhodamine B concentration was used as the base predictors. An engineered predictor set containing nonlinear and interaction descriptors derived from the four experimental variables was also evaluated.

Separate feed-forward networks were developed for the two responses. The hidden layers employed hyperbolic tangent sigmoid activation functions, while a linear activation function was used at output layer. The genetic algorithm optimized number of hidden layers, neurons at all layer and regularization penalty. Each candidate network configuration was encoded as a chromosome and evaluated according to its cross-validated prediction error.

The GA objective function was expressed as:

$$J(\theta) = MSE_{\mathrm{CV}}(\theta) + \lambda_c C(\theta) + \lambda_p\left[\max\left(0, R^2_{\mathrm{target}} - R^2_{\mathrm{CV}}(\theta)\right)\right]^2 \quad \ldots (20)$$

where θ represents the ANN hyperparameters, MSE_{CV} is the cross-validated mean-squared error, $C(\theta)$ is the network-complexity term, and λ_c and λ_p are penalty coefficients. This penalty guided the GA search but did not artificially enforce a predetermined R^2.

The final networks were trained using Levenberg-Marquardt backpropagation with early stopping and regularization. Multiple random initializations were examined, and the network producing the lowest validation error was retained. A 21:3:3 division was used for the final training, validation and testing diagnostic plots. However, model selection and comparison were primarily based on repeated cross-validation because the validation and testing subsets contained only three observations each.

2.12 ANN-GA Performance Evaluation

The predictive accuracy of ANN-GA models was evaluated by the coefficient of determination, correlation coefficient, mean-squared error, root-mean-square error, mean absolute error, and mean absolute percentage error.

$$R^2 = 1 - \frac{\sum_{i=1}^{N}(y_i - \hat{y}_i)^2}{\sum_{i=1}^{N}(y_i - \bar{y})^2} \quad \ldots (21)$$

$$MSE = \frac{1}{N}\sum_{i=1}^{N}(y_i - \hat{y}_i)^2 \quad \ldots (22)$$

$$RMSE = \sqrt{\frac{1}{N}\sum_{i=1}^{N}(y_i - \hat{y}_i)^2} \quad \ldots (23)$$

$$MAE = \frac{1}{N}\sum_{i=1}^{N}|y_i - \hat{y}_i| \quad \ldots (24)$$

$$MAPE(\%) = \frac{100}{N}\sum_{i=1}^{N}\left|\frac{y_i - \hat{y}_i}{y_i}\right| \quad \ldots (25)$$

where $y_i, \hat{y}_i$ and $\bar{y}$ denote the experimental response, ANN-GA prediction, and experimental mean, respectively. Out-of-fold predictions were used to generate regression and error-distribution plots. The ANN-GA results were also compared with leave-one-out quadratic regression to determine whether the nonlinear model improved predictive generalization.

2.13 Confirmation Experiment

Confirmation experiments were performed to verify the Taguchi-predicted factor combination and the best experimental alternative identified by MEREC-MABAC. The Taguchi confirmation condition comprised a contact time of 60 min, solution pH of $10, MnO_2$ /biochar dosage of 0.05 g and initial Rhodamine B concentration of $75 mgL^{-1}$. The MABAC-selected condition was evaluated at 60 min, pH7,0.05 g dosage and $75 mgL^{-1}$ concentration.

Each confirmation condition was independently tested in triplicate under the same temperature, agitation speed, solution volume, and separation procedure applied in the Taguchi L27 experiments. Removal efficiency and adsorption capacity were calculated from the residual Rhodamine B concentration. The confirmation responses were expressed as mean ± standard deviation. Prediction error were calculated using:

$$\text{Prediction error } (\%) = \frac{|y_{\text{exp}} - y_{\text{pred}}|}{y_{\text{exp}}} \times 100 \quad \ldots (26)$$

where y_{exp} and y_{pred} represent the mean confirmation response and predicted value, respectively. An error below 5% was considered satisfactory agreement.

2.14 Adsorption Kinetic Modelling

Time-dependent adsorption data were fitted to five nonlinear kinetic expressions to examine the uptake rate and possible rate-controlling behaviour of Rhodamine B adsorption by the MnO_2 /biochar nanocomposite. The evaluated models were pseudo-first-order, pseudo-second-order, Elovich, intraparticle-diffusion, and fractional-power models. Nonlinear fitting was preferred to avoid errors caused by equation linearization. The mathematical expressions are presented in Table 2.

Table 2. Nonlinear kinetic models applied to Rhodamine B adsorption

S. No.	Kinetic Model	Nonlinear Expression
1	Pseudo-first-order	$q_t = q_e(1 - e^{-k_1 t})$
2	Pseudo-second-order	$q_t = \frac{k_2 q_e^2 t}{1 + k_2 q_e t}$
3	Elovich	$q_t = \frac{1}{\beta}\ln(1 + \alpha\beta t)$
4	Intraparticle diffusion	$q_t = k_{\text{id}} t^{1/2} + C$
5	Fractional power	$q_t = Kt^{v}$

2.15 Equilibrium Isotherm Modelling

Equilibrium adsorption data were analysed using 15 nonlinear isotherm models containing two to five adjustable parameters. These models were selected to evaluate surface homogeneity, adsorption-energy distribution, site saturation and interactions between Rhodamine B and the MnO_2 /biochar nanocomposite. Nonlinear regression was directly applied to q_{v} versus C_{r} clata to avoid errors associated with equation linearization. The corrected model expressions are presented in Table 3.

Table 3. Nonlinear equilibrium models applied to Rhodamine B adsorption

S. No.	Isotherm Model	Nonlinear Equation	References
	Two-parameter Models		
1	Langmuir	$q_x = \frac{q_x K_L C_c}{1 + K_L C_c}$	(Erian *et al.* 2026)

2	Termkin	$q_e = \frac{RT}{b_T} \ln (A_2 C_n)$	(Shirali *et al.* 2026)
3	Freundlich	$q_e - K_y C_l^1 / {}^{(2)}$	(Khedr *et al.* 2026)
4	Dubinin: Radushkevich	$q_e = q_s \exp(-K_{DN} c^2)$	(Hamed *et al.* 2026)
	Three-parameter Models		
5	Khan	$q_e = \frac{q_m b_N C_c}{(1 + b_N C_c)^{sx}}$	(Assefa and Subramaniam, 2025)
6	Jossens	$C_c = \frac{q}{H} \exp(F q_c^2)$	(Chaabane *et al.* 2021)
7	Toth	$q_x = \frac{q_x K_y C_c}{\left[1 + (K_y C_c)^1\right]^{1/y}}$	(Aziam *et al.* 2026)
8	Kohle-Corrigan	$q_e = \frac{A_{NC} C_u^{\text{nec}}}{1 + B_{NC} C_u}$	(Romero *et al.* 2026)
9	Redich Peterson	$q_x = \frac{K_{\parallel} P C_c}{1 + a_{\parallel} P C_s^{\Psi_2}}$	(Beriber *et al.* 2024)
10	Hill	$q_x = \frac{q_x C_x^{n_x}}{K_D + C_e^{D_x}}$	(Simonetti *et al.* 2026)
11	Radke Prausnitz	$q_x = \frac{q_{n\mu} K_{n\nu} C_c}{(1 + K_{n\nu} C_\nu)^{m_{uv}}}$	(Cardoso *et al.* 2011)
12	Sips or Langmur - Freundlich	$q_s = \frac{q_{ns} (K_s C_c)^{n_s}}{1 + (K_5 C_c)^{n_4}}$	(Cardoso *et al.* 2011)
	Four-parameter Models		
13	Baudu	$q_x = \frac{q_x b_x C_x^{1+x+y}}{1 + b_x C_x^{1+z}}$	(Sihag and Pal, 2023)
14	Fritz Schlunder IV	$q_n = \frac{A_{/3} C_c^a}{1 + B_{JS} C_c^G}$	(Nouacer *et al.* 2023)
	Five-parameter Model		
15	Fritz Schlunder V	$q_x = \frac{q_x K_s K_1 C_c^{m_1}}{1 + K_2 C_c^{m_2}}$	(Yahuza *et al.* 2024)

For the Dubinin-Radushkevich model, the Polanyi potential was determined from:

$$\varepsilon = RT \ln \left(1 + \frac{1}{C_e}\right) \quad \ldots (27)$$

where q_e were equilibrium adsorption capacity in mgg^{-1}, C_e were equilibrium Rhodamine B concentration in mgL^{-1} and q_m represents the theoretical maximum adsorption capacity. R and T denote the universal gas constant and absolute temperature, respectively. The remaining terms represent the equilibrium constants, adsorption-intensity coefficients, heterogeneity exponents and empirical parameters associated with their corresponding models.

The parameters of each isotherm were estimated by minimizing the difference between experimental and calculated adsorption capacities. Model performance was evaluated using R^2, RMSE, MAE and other applicable error functions. The most appropriate model was identified from the highest cross-validated R^2 and lowest error values rather than from R^2 alone. A favourable fit was interpreted as a mathematical description of the equilibrium behaviour and not as independent confirmation of a particular adsorption mechanism.

3. RESULTS AND DISCUSSION

3.1 Characterization of the MnO_2/Biochar Nanocomposite

FTIR spectroscopy was employed to identify surface functional groups of pomegranate-peel biochar and MnO_2/biochar nanocomposite. The recorded spectra presented in Fig. 2 is examined to verify MnO_2 incorporation and determine the functional sites potentially responsible for Rhodamine B adsorption.

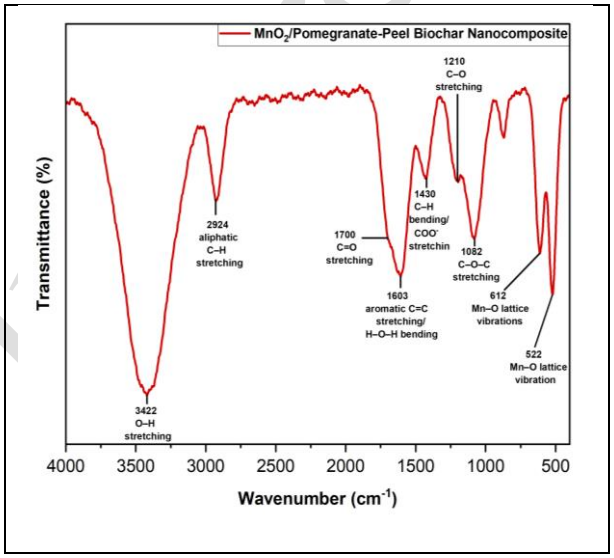

Fig. 2: FTIR spectra of MnO_2/ pomegranate-peel biochar nanocomposite

The FTIR spectra recorded between 4000 and 400 cm^{-1} revealed several oxygen-containing and carbonaceous surface groups. The broad band near 3422 cm^{-1} were assigned to O–H stretching from hydroxyl groups and adsorbed moisture, while peak around 2924 cm^{-1} corresponded to aliphatic C–H stretching. The bands observed at approximately 1700 and 1603 cm^{-1} was associated with C=O stretching and aromatic C=C vibrations. Signal near 1082 cm^{-1} indicated C–O–C stretching from alcohol, ether or phenolic groups. Previous studies have demonstrated that, the FTIR analysis confirmed the successful formation of pomegranate peel-derived hydrochar/titanium dioxide/polypyrrole (PPHC@TiO_2/PPy) through characteristic bands corresponding to oxygen-containing groups, Ti–O–Ti vibrations, and PPy functional groups. The shifts in peak positions and intensities indicated strong interactions among PPHC, TiO_2 nanoparticles, and polypyrrole (Alorabi, 2025). Characteristic bands around

612 and 522 cm^{-1} were attributed to Mn–O lattice vibrations, confirming the incorporation of MnO_2 into the biochar structure. Identified functional groups are summarized in Table 4.

Table 4. Principal FTIR bands of the MnO_2 /biochar nanocomposite

Wavenumber (cm^{-1})	Functional-group Assignment
612 and 522	Mn-O lattice vibration
1082	C–O–C stretching
1430	C – H bending
1603	Aromatic C=C stretching
1700	C=O stretching
2924	Aliphatic C-H stretching
3422	O-H stretching

The UV-Vis spectrum of the MnO_2 /biochar nanocomposite is presented in Fig. 3. An absorption feature within approximately $268 - 270$ nm was associated with $\pi \rightarrow \pi^*$ transitions of aromatic carbon structures. The shoulder extending into the $310 - 400$ nm region was attributed to $n \rightarrow \pi^*$ transitions involving carbonyl groups. Broad absorption at higher wavelengths was associated with electronic transitions involving $Mn - O$ species. These optical features further supported the successful integration of MnO_2 with the pomegranate-peel-derived biochar.

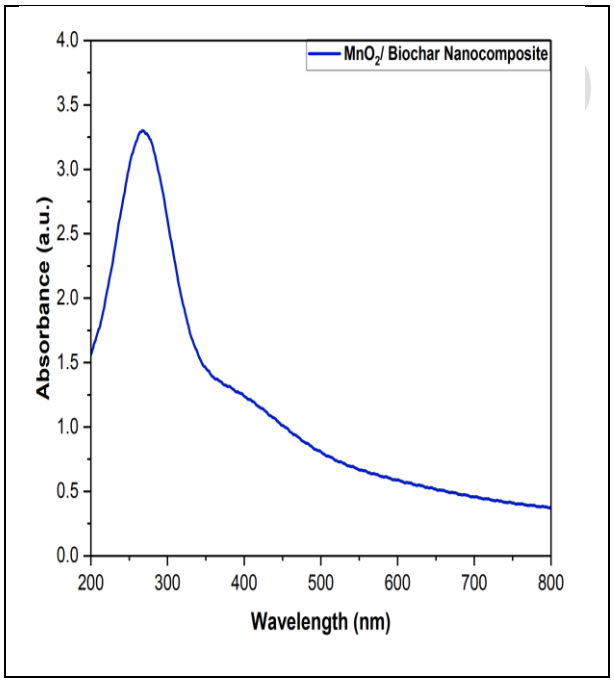

Fig. 3: UV–Vis absorption spectrum of the MnO_2/biochar nanocomposite

Figure 4 presents FESEM micrographs of the prepared nanocomposite recorded at different magnifications.

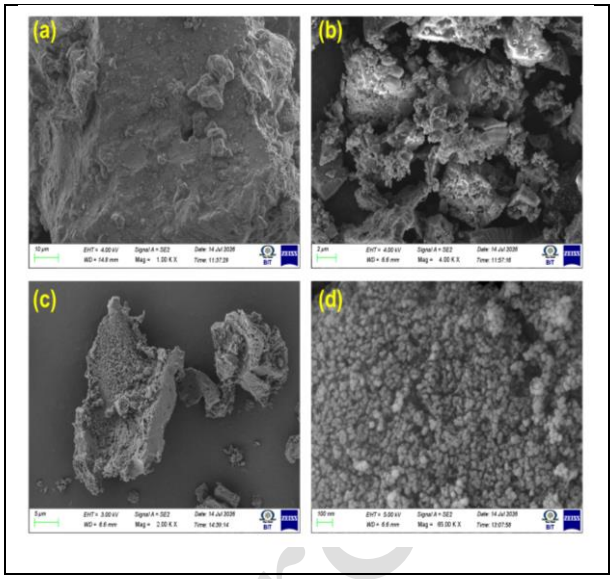

Fig. 4: FESEM micrographs of the MnO_2/biochar nanocomposite at different magnifications

The micrographs displayed an irregular, coarse surface containing cavities, void spaces, and minor fractures. Many granular deposits and agglomerates were scattered on the biochar matrix. It was attributed to the MnO_2 particles in these deposits, which would be confirmed through EDS elemental analysis. The resulting irregular and porous structure may offer the site for binding and ensure the diffusion of Rhodamine B into adsorbent structure. In prior research, SEM analysis revealed that the pomegranate peel powder/reduced graphene oxide (PPP/rGO) nanocomposite possessed a rough, porous, and heterogeneous surface with PPP particles distributed across wrinkled rGO sheets. This morphology provided abundant active sites and enhanced the adsorption of Pb (II) ions and methylene blue (MB) (Hassan *et al.* 2025). The crystalline characteristics of the prepared nanocomposite were subsequently evaluated from the XRD pattern presented in Fig. 5.

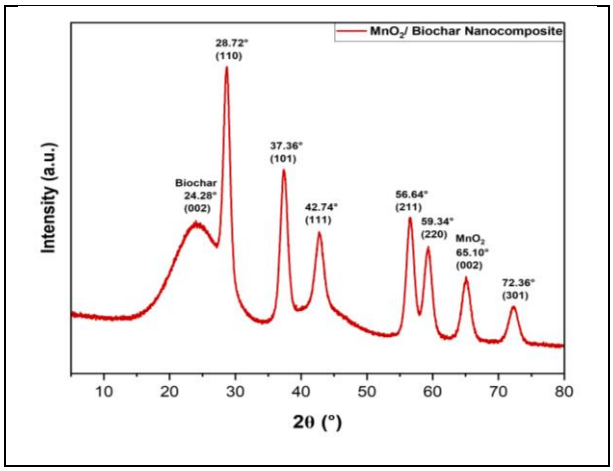

Fig. 5: PXRD pattern of the MnO_2/biochar nanocomposite

The diffraction peaks at 2θ = 28.72°, 37.36°, 42.74°, 56.64°, 59.34°, 65.10°, and 72.36° were indexed to the (110), (101), (111), (211), (220), (002), and (301) planes of tetragonal β-MnO_2, respectively, consistent with ICDD/JCPDS card No. 24-0735. The broad band near 24.28° was attributed to the (002) plane of disordered carbon. The agreement between the experimental reflections and the reference pattern confirms crystalline β-MnO_2 within the predominantly amorphous biochar matrix. In prior research, XRD analysis confirmed the successful intercalation of hexadecylpyridinium bromide (HDPy) into purified Tunisian smectite clay at 0.5CEC, 1CEC, and 2CEC levels. The increased basal spacing indicated expansion of the clay interlayers and successful formation of the HDPy-modified organoclays (Saad *et al.* 2025).

3.2 Brunauer-Emmett-Teller Analysis

Specific surface area, pore-size characteristics, and pore volume of MnO_2 /biochar nanocomposite was obtained from the nitrogen adsorption-desorption isotherm presented in Fig. 6.

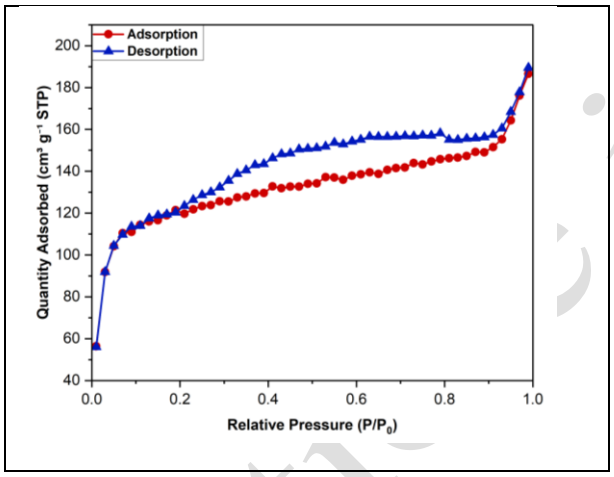

Fig. 6: Nitrogen adsorption–desorption isotherm of the MnO_2/biochar nanocomposite

The adsorption–desorption profile exhibited a Type IV isotherm with a distinct hysteresis loop, confirming the predominantly mesoporous character of the nanocomposite. The mean pore diameter of 2.81 nm lies within the mesoporous range of 2–50 nm. The material exhibited a surface area of 412.834 $m^2\ g^{-1}$, a Langmuir surface area of 672.0659 $m^2\ g^{-1}$, and a total pore volume of 0.289 $cm^3\ g^{-1}$. The developed porous structure shows accessible diffusion pathways and numerous surface sites for Rhodamine B adsorption. The nitrogen-sorption parameters are summarized in Table 5.

Table 5. Textural characteristics of the MnO_2/biochar nanocomposite

Parameter	Measured Value
BET surface area ($m^2\ g^{-1}$)	412.834
Langmuir surface area ($m^2\ g^{-1}$)	672.0659
Total pore volume ($cm^3\ g^{-1}$)	0.289
Mean pore diameter (nm)	2.81

3.3 Taguchi Optimization of Adsorption Capacity

Taguchi L27 orthogonal array was employed to evaluate the influence of contact time, solution pH, MnO_2/biochar dosage, and initial Rhodamine B concentration. Adsorption capacity was analysed using the larger-the-better signal-to-noise criterion because a higher dye uptake per unit mass of adsorbent was desirable. The resulting S/N response values are presented in Table 6.

Table 6. Response table for larger-the-better S/N ratios

Level	Contact Time	Solution pH	MnO_2/PPB Dosage	Initial RhB Concentration
1	33.62	34.44	36.71	32.58
2	34.93	33.83	34.78	34.69
3	35.09	35.38	32.16	36.38
Delta	1.47	1.55	4.54	3.80
Rank	4	3	1	2

The MnO_2/biochar dosage generated the highest S/N delta of 4.54 and was therefore ranked as the most influential factor. Initial concentration occupied the second position with a delta of 3.80, followed by solution pH and contact time. The maximum S/N values were obtained at 60 min, pH 10, 0.05 g dosage and 75 mg L^{-1} initial concentration. This combination was consequently identified as the Taguchi-predicted condition for achieving a robust adsorption capacity.

The mean-response results are provided in Table 7. Adsorption capacity increased from 57.65 to 65.03 mg g^{-1} as contact time increased from 20 to 60 min. A similar positive effect was observed for initial concentration, for which the mean capacity increased from 56.44 to 68.38 mg g^{-1}. In contrast, increasing dosage from 0.05 to 0.15 g reduced mean capacity from 70.30 to 55.13 mg g^{-1}.

Table 7. Response table for mean adsorption capacity

Level	Contact Time	Solution pH	MnO_2/PPB Dosage	Initial RhB Concentration
1	57.65	58.99	70.30	56.44
2	63.70	62.36	60.96	61.56
3	65.03	65.04	55.13	68.38
Delta	7.38	6.05	15.16	11.94
Rank	3	4	1	2

The inverse relationship between adsorbent dosage and mass-normalized capacity can be attributed to incomplete utilization of available binding sites at

higher solid loadings. The increased adsorbent mass can also promote particle aggregation and reduce effective surface area accessible to each dye molecule. The mean-response ranking identified dosage as the dominant variable, followed by concentration, contact time, and pH.

The main-effects plot for the mean response is presented in Fig. 7. The steep negative slope associated with dosage confirms its strong influence on adsorption capacity. Contact time, solution pH, and initial concentration exhibited positive trends, although the increase in capacity became less pronounced between 40 and 60 min.

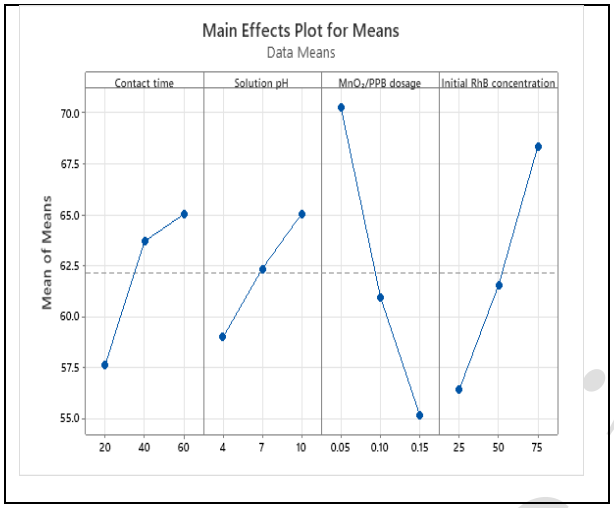

Fig. 7: Main-effects plot for mean adsorption capacity

The S/N main-effects plot in Fig. 8 displayed trends consistent with the arithmetic means. The highest robust response occurred at the third level of contact time, third level of pH, first level of dosage and third level of concentration. Agreement between the mean and S/N plots indicates that the selected levels improved both the magnitude and consistency of adsorption capacity.

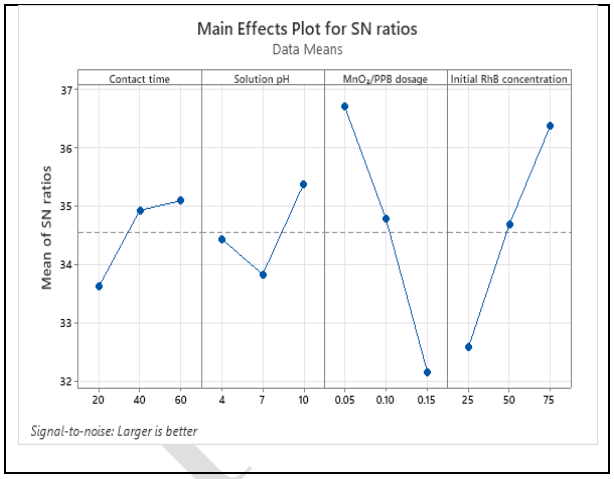

Fig. 8: Main-effects plot for larger-the-better S/N ratios

3.4 Analysis of Variance

ANOVA was conducted separately for Rhodamine B removal efficiency and adsorption capacity. The ANOVA results for removal efficiency are shown in Table 8 and Fig. 9. All four variables were statistically significant at $p<0.001$.

Table 8. ANOVA results for Rhodamine B removal efficiency

Source	DF	Seq SS	Contribution (%)	Adj SS	Adj MS	F -value	p-value
Contact time	2	226.14	40.37	226.14	113.071	116.60	<0.001
Solution pH	2	164.89	29.44	164.89	82.443	85.02	<0.001
MnO_2/PPB dosage	2	64.74	11.56	64.74	32.371	33.38	<0.001
Initial RhB concentration	2	86.93	15.52	86.93	43.466	44.82	<0.001
Error	18	17.46	3.12	17.46	0.970	-	-
Total	26	560.16	100.00	-	-	-	-

Contact time was the main factor affecting removal efficiency, accounting for 40.37% of the total variation. Solution pH contributed 29.44%, while initial concentration and adsorbent dosage contributed 15.52% and 11.56%, respectively. The residual contribution was limited to 3.12%, indicating that the selected experimental variables explained 96.88% of the variability in removal efficiency.

Adsorption capacity exhibited a substantially different factor hierarchy as presented in Table 9. Adsorbent dosage was the predominant factor, contributing 56.26% of the response variation. Initial concentration accounted for 37.50%, whereas contact time and pH contributed only 3.74% and 1.76%, respectively.

Table 9. ANOVA results for Rhodamine B adsorption capacity

Source	DF	Seq SS	Contribution (%)	Adj SS	Adj MS	F -value	p-value
Contact time	2	353.79	3.74	353.79	176.89	45.58	<0.001
Solution pH	2	166.58	1.76	166.58	83.29	21.46	<0.001
MnO_2/PPB dosage	2	5322.43	56.26	5322.43	2661.22	685.71	<0.001
Initial RhB concentration	2	3547.66	37.50	3547.66	1773.83	457.06	<0.001
Error	18	69.86	0.74	69.86	3.88	-	-
Total	26	9460.32	100.00	-	-	-	-

The very small error contribution of 0.74% demonstrates that the experimental factors accounted for 99.26% of the variation in adsorption capacity. The contrasting ANOVA results indicate that high removal efficiency and high adsorption capacity were controlled by different factor combinations. Consequently, simultaneous multi-response optimization was necessary. Earlier studies, CCD–RSM supported by ANOVA was applied to optimize crystal violet removal using Sn–Fe- and Sn–Zn-modified pomegranate-peel biosorbents. The optimized adsorption capacities were 675.47 and 357.18 mg g^{-1}, respectively (Hamrouche *et al.* 2026).

3.5 MEREC Objective Weighting

MEREC was employed to calculate objective weights for removal efficiency and adsorption capacity without introducing subjective preferences. The removal effect and resulting criterion weights are presented in Table 10.

Table 10. MEREC removal effects and objective weights

Criterion	Removal Effect	MEREC Weight
Removal efficiency	1.1837	0.1071
Adsorption capacity	9.8718	0.8929

Adsorption capacity exhibited a removal effect of 9.8718 and received a weight of 0.8929. Removal efficiency produced a smaller effect of 1.1837 and was assigned a weight of 0.1071. The weights indicate that eliminating adsorption capacity caused the greatest disturbance to the overall performance of the alternatives. Therefore, adsorption capacity exerted the greatest influence on the subsequent MABAC ranking.

3.6. MABAC Ranking of Experimental Alternatives

The MEREC weights were incorporated into MABAC to obtain a combined performance score for every Taguchi run. Positive scores indicate alternatives positioned above the border approximation area, whereas negative scores indicate comparatively weaker performance. The ten highest-ranking experimental conditions are listed in Table 11.

Table 11. Leading alternatives obtained from MEREC–MABAC analysis

Run	Time (min)	pH	Dose (g)	C_0 (mgL^{-1})	Removal (%)	Capacity (mgg^{-1})	MABAC score	Rank
24	60	7	0.05	75	74.50	85.53	0.47995	1
23	40	7	0.05	75	70.01	87.60	0.47876	2
18	60	10	0.05	50	78.30	76.80	0.39208	3
22	20	7	0.05	75	66.54	76.40	0.31483	4
17	40	10	0.05	50	74.52	71.81	0.30533	5
16	20	10	0.05	50	72.16	64.37	0.19609	6
11	40	4	0.10	75	71.24	61.68	0.15619	7

12	60	4	0.10	75	73.89	58.97	0.13793	8
8	40	10	0.15	75	79.57	54.37	0.11420	9
3	60	4	0.05	25	75.30	53.02	0.07080	10

Run 24 achieved the highest MABAC score of 0.47995 and was identified as the best experimentally tested alternative. This experiment combined 60 min contact time, pH 7, 0.05 g dosage, and 75 mg L^{-1} initial concentration, producing 74.50% removal and 85.53 mg g^{-1} adsorption capacity.

Run 23 produced a slightly higher adsorption capacity of 87.60 mg g^{-1} but a lower removal efficiency of 70.01%. Its resulting MABAC score of 0.47876 was marginally below that of Run 24. The result shows that Run 24 represented the most favourable compromise between the two responses rather than the maximum individual value of either response.

The Taguchi factor-level prediction and MABAC ranking should be distinguished. Taguchi identified 60 min, pH 10, 0.05 g and 75 mg L^{-1} as the preferred factor-level combination, whereas MABAC selected Run 24 from the conditions experimentally included in the L27 array. The Taguchi-predicted combination must therefore be evaluated through an independent confirmation experiment before being reported as the experimentally validated optimum.

3.7 ANN–GA Model Development and Comparison

ANN–GA models were developed using the four experimental variables and an expanded set containing engineered nonlinear and interaction predictors. Separate networks were trained for removal efficiency and adsorption capacity. The fitted and cross-validated performance values are summarized in Table 12.

Table 12. Predictive performance of the regularized ANN–GA models

Response	Fitted (R^2)	Cross-Validated (R^2)	CV RMSE	Quadratic LOO (R^2)
Removal efficiency	0.9692	0.8352 ± 0.0143	1.8474	0.9265
Removal efficiency	0.9682	0.8488 ± 0.0382	1.7593	0.9265
Adsorption capacity	0.9836	0.8735 ± 0.0609	6.5063	0.9777
Adsorption capacity	0.7517	0.9173 ± 0.0631	5.1345	0.9777

For removal efficiency, the engineered predictor set increased the cross-validated R^2 from 0.8352 to 0.8488 and reduced RMSE from 1.8474 to 1.7593% points. The fitted R^2 of 0.9682 was higher than its cross-validated value, indicating that the network described the training observations more accurately than unseen data.

The experimental and out-of-fold ANN–GA predictions for removal efficiency are compared in Fig. 9. Most predictions followed the identity line, although deviations were visible at the upper response range. The error bars indicate variation among the repeated cross-validation predictions.

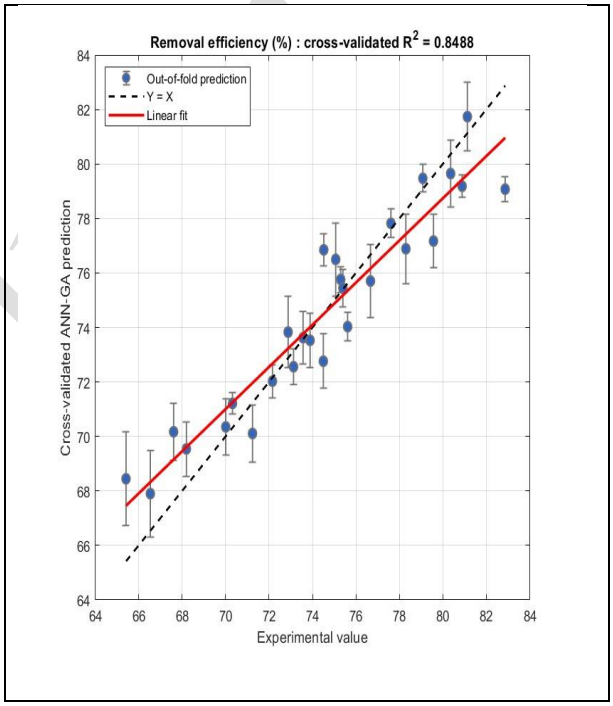

Fig. 9: Experimental and cross-validated ANN–GA predictions for removal efficiency

For adsorption capacity, the engineered inputs improved cross-validated R^2 from 0.8735 to 0.9173 and reduced RMSE from 6.5063 to 5.1345 mg g^{-1}. Although the engineered model produced the best cross-validated result, its fitted R^2 of 0.7517 indicated instability in the final network realization. Therefore, the cross-validated predictions provide a more reliable assessment than the single fitted model.

Figure 10 presents the experimental and cross-validated adsorption-capacity predictions. The model captured the general response trend, but wider error bars were observed around the extreme capacity values.

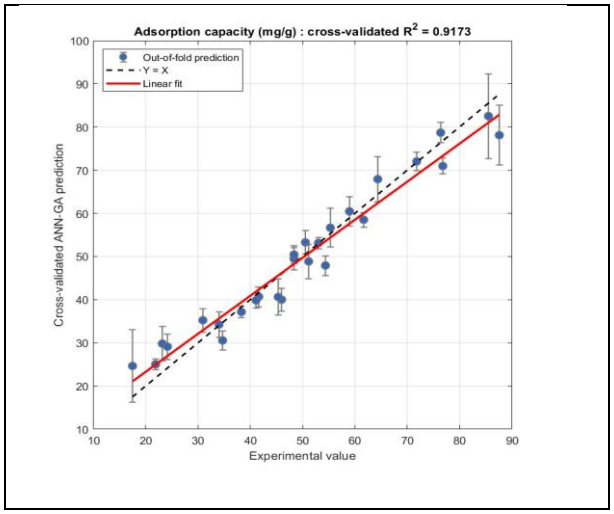

Fig. 10: Experimental and cross-validated ANN–GA predictions for adsorption capacity

Quadratic regression achieved leave-one-out R^2 values of 0.9265 for removal efficiency and 0.9777 for adsorption capacity. These values exceeded the corresponding ANN–GA cross-validated results. Thus, ANN–GA successfully captured nonlinear relationships but did not outperform quadratic regression in predicting unseen observations from the limited L27 dataset. In prior studies, FCCD–RSM and ANN–GA were employed to optimize microwave power and vacuum pressure during pomegranate-peel drying. ANN–GA provided greater predictive accuracy and optimum conditions of 287 W and 19 kPa (Elnjikkal and Dwivedi, 2022). The machine-learning results should be interpreted cautiously because the dataset comprised only 27 Taguchi experiments, with three observations each for validation and testing. The engineered ANN–GA models achieved cross-validated R^2 values of 0.8488 and 0.9173 for removal efficiency and adsorption capacity, respectively. However, quadratic regression exhibited higher leave-one-out R^2 values of 0.9265 and 0.9777, indicating better generalization for the limited dataset. Therefore, ANN–GA performance should be considered preliminary and validated using a larger independent dataset.

3.8 Analysis of ANN–GA Performance Functions

The training, validation, testing and overall performance functions obtained from the final data partition are presented in Table 13.

Table 13. Performance functions of the final ANN–GA models

Response	Subset	Samples	MSE	RMSE	(R^2)
Removal efficiency	Training	21	0.3272	0.5720	0.9924
Removal efficiency	Validation	3	0.1249	0.3535	0.9915
Removal efficiency	Testing	3	2.1192	1.4557	0.9605
Removal efficiency	Overall	27	0.5038	0.7098	0.9880
Adsorption capacity	Training	21	175.63	13.253	0.7198
Adsorption capacity	Validation	3	1.5042	1.2265	0.9998
Adsorption capacity	Testing	3	69.015	8.3076	0.9849
Adsorption capacity	Overall	27	144.44	12.018	0.7731

The removal-efficiency network exhibited strong correlations in the training, validation, and testing subsets. Its overall RMSE was 0.7098%, with an overall correlation coefficient of 0.9880. Nevertheless, the validation and testing subsets contained only three observations each; consequently, their high correlation values should be interpreted cautiously.

The adsorption-capacity model exhibited a training RMSE of 13.253 mg g^{-1} and an overall correlation coefficient of 0.7731. Although the validation and testing correlations were high, they were calculated using only three observations per subset and did not reflect the broader model error. Repeated cross-validation therefore remained the primary basis for evaluating predictive performance.

3.9 ANN–GA Error Distribution

The prediction-error histogram for removal efficiency is presented in Fig. 11. Most errors were concentrated close to zero, indicating reasonable agreement between experimental and modelled values. Only a small number of observations occurred in the outer error intervals.

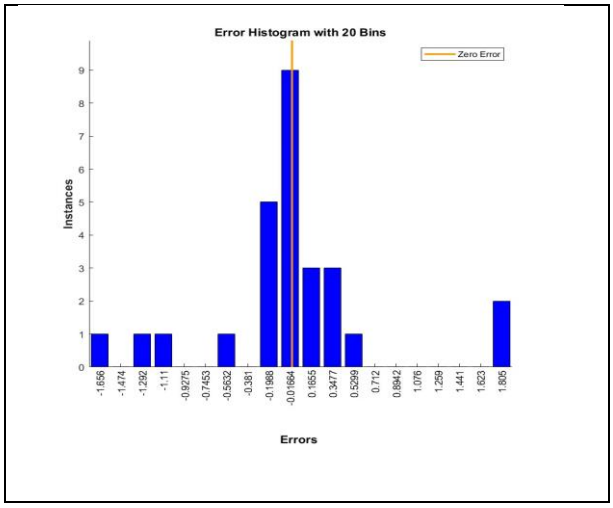

Fig. 11: ANN–GA error histogram for removal efficiency

The adsorption-capacity error distribution shown in Fig. 12 was considerably broader and extended from approximately −20.85 to 19.96 mg g^{-1}. This wider distribution confirms that adsorption capacity was more difficult to predict than removal efficiency. The largest deviations were associated with experimental regions displaying abrupt changes in capacity caused by dosage and concentration effects.

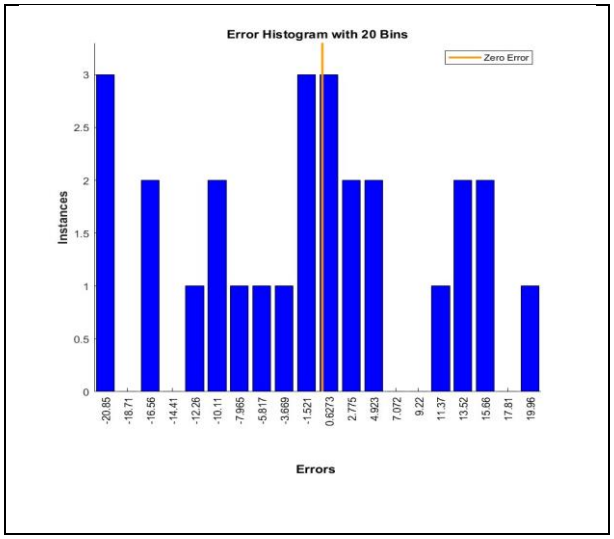

Fig. 12: ANN−GA error histogram for adsorption capacity

3.10 Confirmation of Optimized Adsorption Conditions

The confirmation results for the Taguchi-predicted and MABAC-selected conditions are presented in Table 14. At the Taguchi condition of $60\ \text{min}, \text{pH}10, 0.05\ \text{g}$ dosage and 75mgL^{-1} concentration, the confirmation experiment produced a removal efficiency of $76.80 \pm 0.24\%$ and an adsorption capacity of $87.63 \pm 0.41\ \text{mgg}^{-1}$. These responses were close to the predicted values of 76.90% and 87.83mgg^{-1}, corresponding to errors of only 0.13% and 0.23%, respectively.

Repetition of the MABAC-selected condition at $60\ \text{min}, \text{pH}7, 0.05\ \text{g}$ and 75mgL^{-1} produced $74.51 \pm 0.22\%$ removal efficiency and $85.53 \pm 0.38\text{mgg}^{-1}$ adsorption capacity. These values closely agreed with the original Run 24 responses of 74.50% and 85.53mgg^{-1}. The corresponding errors were 0.02% and 0.00%.

Table 14. Comparison of predicted and confirmed adsorption responses

Optimized Condition	Predicted Value	Confirmation Value (Mean ± SD)	Error (%)
Taguchi: 60 min, pH 10, 0.05 g, 75 mg L^{-1}	76.90	76.80 ± 0.24	0.13
Taguchi: 60 min, pH 10, 0.05 g, 75 mg L^{-1}	87.83	87.63 ± 0.41	0.23
MABAC: 60 min, pH 7, 0.05 g, 75 mg L^{-1}	74.50	74.51 ± 0.22	0.02
MABAC: 60 min, pH 7, 0.05 g, 75 mg L^{-1}	85.53	85.53 ± 0.38	0.00

All prediction errors were substantially below the predefined 5% acceptance limit, demonstrating close agreement between the predicted and confirmation responses. The Taguchi condition delivered the highest simultaneous values of removal efficiency and adsorption capacity, whereas the MABAC result validated Run 24 as the best condition among the original L27 experiments. Therefore, $60\ \text{min}, \text{pH}10, 0.05\ \text{g}$ dosage and 75mgL^{-1} initial concentration can be selected as the final optimized condition

3.11 Batch Adsorption Kinetics

Figure 13 presents the nonlinear fitting of the PFO, PSO, Elovich, intraparticle diffusion, and fractional-power models used to describe Rhodamine B uptake by the MnO_2/biochar nanocomposite.

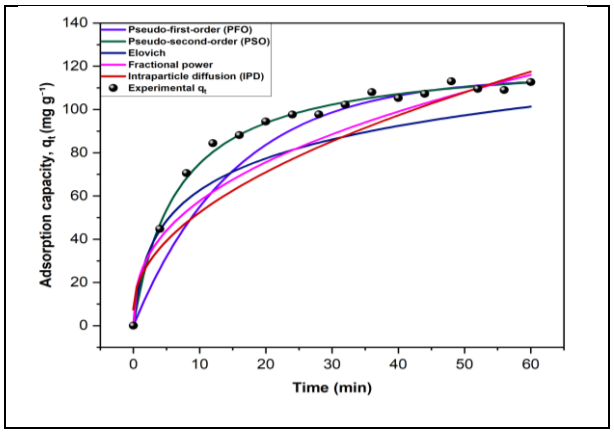

Fig. 13: Nonlinear kinetic-model fitting for Rhodamine B adsorption onto the MnO_2/biochar nanocomposite

The kinetic equations were applied to identify the probable uptake pathway and rate-controlling stage of Rhodamine B adsorption by the MnO_2/biochar nanocomposite. Table 15 summarizes the fitted constants and statistical error indicators used for model selection.

Table 15. Nonlinear kinetic parameters and goodness-of-fit indicators for Rhodamine B adsorption

Entry	Model	Estimated parameters	R^2	χ^2	HYBRID	ARE	ERRSQ	RMSE	MPSD
1	PFO	q_e = 117.642 ± 1.284 mg g^{-1}; k_1 = 0.0648 ± 0.0037 min^{-1}	0.9892	0.364	4.106	3.124	4.732	0.648	4.286
2	PSO	q_e = 130.410 ± 1.160 mg g^{-1}; k_2 = (7.81 ± 0.47) × 10^{-4} g mg^{-1} min^{-1}	0.9973	0.106	1.204	1.482	1.286	0.338	1.936
3	Fractional power	K = 35.720 ± 0.842; v = 0.2865 ± 0.0086	0.9701	0.688	8.917	5.932	8.436	0.866	7.814
4	Elovich	α = 26.800 ± 1.574 mg g^{-1} min^{-1}; β = 0.0418 ± 0.0026 g mg^{-1}	0.9786	0.521	6.742	4.816	6.308	0.771	6.237
5	IPD	K_{diff} = 14.850 ± 0.436 mg g^{-1} $min^{-0.5}$; C = 1.800 ± 0.684 mg g^{-1}	0.9624	0.847	12.106	7.246	11.642	1.017	9.518

Every model produced an R^2 above 0.96, indicating an acceptable representation of the experimental kinetic behaviour. The PFO equation yielded the highest R^2 (0.9892), with q_e = 117.642 mg g^{-1} and k_1 = 0.0648 min^{-1}. However, its larger error indices prevented its selection solely based on the correlation coefficient. The PSO model produced R^2 = 0.9973, q_e = 130.410 mg g^{-1}, k_2 = 0.000781 g mg^{-1} min^{-1}. Recorded the lowest χ^2, HYBRID, ERRSQ, ARE, RMSE, and MPSD values, demonstrating the closest overall agreement with the observations.

The fractional-power fit (R^2 = 0.9701) reflected the time-dependent and heterogeneous nature of Rhodamine B uptake. The Elovich result (R^2 = 0.9786) further ssuggested adsorption on energetically nonuniform active sites. For the IPD model, K_{diff} was 14.850 mg g^{-1} $min^{-0.5}$, and the nonzero intercept was 1.800 mg g^{-1}. Because its fitted line did not pass through the origin, intraparticle diffusion contributed to adsorption but was not the only rate-controlling mechanism. Considering all statistical indicators together, PSO gave the strongest kinetic description, suggesting that surface interactions substantially governed Rhodamine B uptake by the MnO_2/biochar nanocomposite. Nevertheless, kinetic-model agreement alone does not conclusively prove chemisorption and should be interpreted alongside characterization and equilibrium evidence.

3.12 Equilibrium Adsorption Isotherms

Equilibrium isotherms describe how Rhodamine B is distributed between the aqueous phase and the MnO_2/biochar nanocomposite surface. Agreement between measured and model-estimated data was evaluated to clarify the adsorption behaviour. The equations were grouped into two-, three-, four-, and five-parameter models. The two-parameter models were examined first, as presented in Fig. 14.

Nonlinear fitting of two-parameter isotherm models for Rhodamine B adsorption onto the MnO_2/biochar nanocomposite.

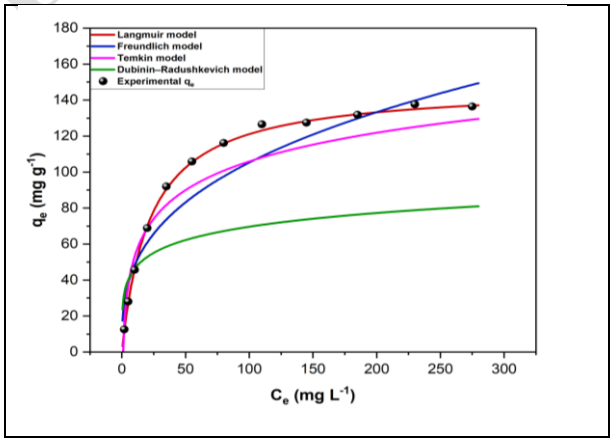

Fig. 14: Nonlinear fitting of two-parameter equilibrium models for Rhodamine B adsorption

The fitted curves indicated close agreement between the calculated and measured equilibrium data. The estimated constants, R^2 values and error statistics for two-parameter equations were summarized on Table 16.

Table 16. Two-parameter isotherm constants and statistical error indicators

Entry	Isotherm	Estimated Metrics	R^2	x^2	HYBRID	ARE	ERRSQ	RMSE	MPSD
1	Langmuir	q_{max} = 144.8515 ± 1.3036 mg g^{-1}; KL = 0.0553 ± 0.0023 L mg^{-1}	0.9981	0.084	2.106	1.986	1.842	0.592	2.814

2	Freundlich	KF = 20.1842 ± 1.1264 (mg g⁻¹)(L mg⁻¹)^(1/n); 1/n = 0.3551 ± 0.0082	0.9638	0.536	9.482	5.634	8.927	1.286	7.218
3	Temkin	AT = 1.1152 ± 0.2012 L g⁻¹; BT = 24.8404 ± 1.0799 mg g⁻¹	0.9814	0.318	6.217	4.182	5.846	0.946	5.763
4	DubininRadushkevich	qm = 82.4168 ± 4.7261 mg g⁻¹; KDR = 0.0026 ± 0.0002 mol² kJ⁻²; E = 13.8883 kJ mol⁻¹	0.8085	0.972	23.174	8.264	174.286	2.316	11.972

Langmuir, Freundlich, and Temkin provided considerably better fits than the Dubinin–Radushkevich equation. Langmuir produced the highest R^2 of 0.9981 and estimated maximum monolayer capacity of 144.8515 mg g^{-1}. Freundlich exponent, $1/n$ = 0.3551, was between zero and one, indicating favourable Rhodamine B uptake on an energetically heterogeneous surface. Its lower χ^2, ERRSQ, HYBRID, RMSE, and MPSD values demonstrated the smallest overall prediction error. The Temkin model also achieved a high R^2 of 0.9814, suggesting that adsorption energy changed as surface coverage increased. By contrast, the Dubinin–Radushkevich model showed relatively weak agreement, with R^2 = 0.8085 and the largest error values.

Considering R^2 alone, Langmuir was superior, whereas the combined error criteria favoured Freundlich. The equilibrium behaviour may therefore involve strong adsorption on nonuniform sites rather than an exclusively ideal monolayer process. Additional three-parameter equations were subsequently assessed to describe this surface heterogeneity more comprehensively, as illustrated in Fig. 15.

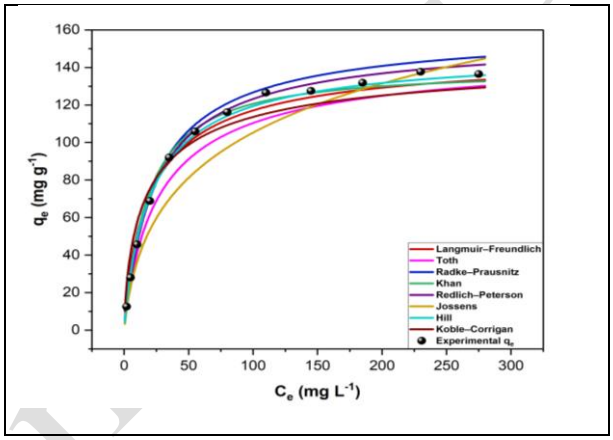

Fig. 15: Nonlinear fitting of three-parameter isotherm models for Rhodamine B adsorption

The fitted profiles showed reasonable agreement between the experimental adsorption capacity and model-estimated equilibrium values. Table 17 presents the fitted constants, determination coefficients, and available error statistics for the three-parameter equations.

Table 17. Three-parameter isotherm constants and error indicators

Entry	Isotherm	Estimated Parameters	X^2	$\mathbb{R}^+$	HYBRID	ARE	ERRSQ	RMSE	MPSD
1	Langmuir Freundlich	qm = 142.360 ± 3.210 mg g⁻¹; K = 0.0541 ± 0.0042 L mg⁻¹; n = 0.8924 ± 0.0415	0.116	0.9962	2.132	1.936	1.684	0.574	3.106
2	Toth	qm = 148.720 ± 4.840 mg g⁻¹; K = 0.0618 ± 0.0051 L mg⁻¹; τ = 0.7365 ± 0.0384	0.184	0.9938	2.984	2.317	2.426	0.689	3.784
3	Racke Prausnitz	qm = 154.310 ± 5.260 mg g⁻¹; K = 0.0492 ± 0.0047 L mg⁻¹; n = 0.8621 ± 0.0436	0.362	0.9856	5.684	3.286	4.918	0.923	5.194
4	Khan	qm = 141.680 ± 3.470 mg g⁻¹; K = 0.0637 ± 0.0049 L mg⁻¹; n = 0.9138 ± 0.0397	0.092	0.9971	1.786	1.724	1.324	0.508	2.846
5	Redlich-Peterson	KRP = 18.460 ± 0.742 L g⁻¹; aRP = 0.1324 ± 0.0096 (L mg⁻¹)^n; β = 0.8427 ± 0.0318	0.138	0.9954	2.418	2.064	1.936	0.615	3.362

6	Jossens	KJ = 16.250 ± 0.684; j = 0.0823 ± 0.0067; n = 0.7116 ± 0.0462	0.584	0.9678	8.936	4.276	7.862	1.167	6.842
7	Hill	qm = 143.820 ± 3.960 mg g^{-1}; K = 18.720 ± 1.284 mg L^{-1}; n = 0.8354 ± 0.0526	0.157	0.9946	2.762	2.183	2.146	0.647	3.587
8	Koble Comigan	A = 8.426 ± 0.618; B = 0.0417 ± 0.0041; n = 0.6842 ± 0.0448	0.126	0.9958	2.286	1.984	1.792	0.592	3.218

Based on R^2, the fitting order was Khan > Langmuir–Freundlich > Koble–Corrigan > Redlich–Peterson > Hill > Toth > Radke–Prausnitz > Jossens. The Toth exponent below unity indicated deviation from an ideal uniform surface, although the large uncertainty associated with its estimated capacity suggests weak parameter identifiability. Redlich–Peterson produced R^2 = 0.9971 and comparatively low HYBRID, RMSE, ARE, and MPSD values, providing the most statistically balanced description. Its exponent of 0.8427 reflected behaviour intermediate between ideal Langmuir and heterogeneous Freundlich adsorption.

Langmuir–Freundlich model also fitted measurements closely, supporting concentration-dependent adsorption on nonuniform active sites. Khan and Radke–Prausnitz provided acceptable representations of combined homogeneous and heterogeneous behaviour. Hill indicated possible cooperative interaction, whereas Jossens and Koble–Corrigan represented adsorption across binding sites with different energies. However, high R^2 values alone do not establish a particular surface mechanism, particularly where error statistics are unavailable.

Overall, the three-parameter analysis supports heterogeneous Rhodamine B adsorption by the MnO_2/biochar nanocomposite, agreeing with the earlier Freundlich interpretation. The four-parameter Fritz–Schlunder IV and Baudu equations and the five-parameter Fritz–Schlunder V model was subsequently evaluated, as illustrated in Fig. 16.

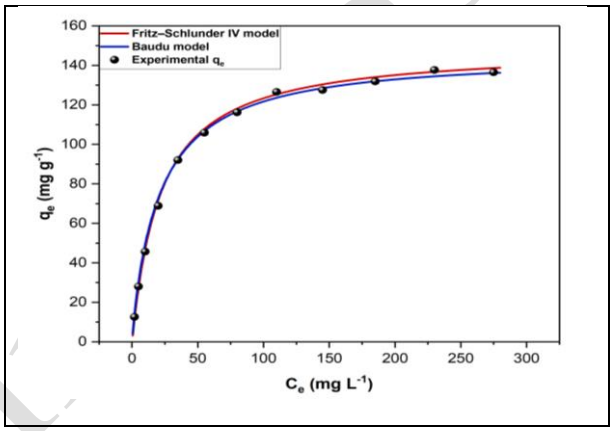

Fig. 16: Nonlinear fitting of four-parameter isotherm models for Rhodamine B adsorption

Both four-parameter equations closely reproduced the measured equilibrium profile. Their fitted constants, determination coefficients and statistical error indicators are provided in Table 18.

Table 18. Four-parameter isotherm constants and error indicators

Entry	Isotherm	Estimated Parameters	R^2	χ^2	HYBRID	ERRSQ	ARE	RMSE	MPSD
1	Fritz-Schlunder IV	A = 18.7624 ± 1.6842; m = 0.9421 ± 0.0486; B = 0.1286 ± 0.0094; n = 0.7914 ± 0.0327	0.9984	0.076	1.842	1.386	1.486	0.372	2.374
2	Baudu	qm = 143.8260 ± 3.2140 mg g^{-1}; K = 0.0614 ± 0.0047; A = 0.8427 ± 0.0382; B = 0.1268 ± 0.0091	0.9942	0.138	2.936	2.428	1.982	0.493	3.126

The high R^2 values obtained for Fritz–Schlunder IV and Baudu demonstrated close agreement between their predictions and the experimental observations. Model suitability was further compared using χ^2, ERRSQ, HYBRID, RMSE, ARE and MPSD, for which smaller values indicate reduced prediction error. Fritz–Schlunder IV produced the highest R^2 of 0.9984 and lower values for most error criteria, including χ^2, ERRSQ, HYBRID, RMSE and ARE. It therefore gave the stronger overall four-parameter fit and indicated adsorption across energetically nonuniform sites.

The Baudu equation also described the equilibrium data adequately, with R^2 = 0.9942. However,

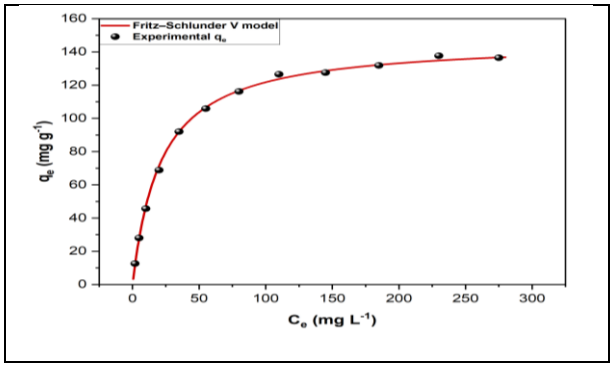

Fig. 17: Nonlinear fitting of the five-parameter Fritz–Schlunder V isotherm for Rhodamine B adsorption

Figure 17 shows that the Fritz–Schlunder V equation reproduced the measured equilibrium trend. Its fitted constants, R^2, and error indicators are summarized in Table 19. its estimated capacity of 143.8260 mg g^{-1} was substantially lower than the Langmuir maximum of 144.8515 mg g^{-1}, limiting its physical representation of the observed adsorption capacity. The four-parameter comparison consequently favoured Fritz–Schlunder IV and supported heterogeneous equilibrium behaviour. Nevertheless, a complex model should be accepted only when its improved fit justifies the additional parameters. The five-parameter Fritz–Schlunder V equation was finally examined, as presented in Fig. 17.

Table 19. Fritz–Schlunder V and error indicators

Entry	Isotherm	Estimated Parameters	x^2	HYBRID	R^2	ERRSQ	ARE	RMSE	MPSD
1	Fritz-Schlunder V	qm = 145.2860 ± 3.1840 mg g^{-1}; K1 = 0.0548 ± 0.0036; m = 0.9142 ± 0.0427; K2 = 0.0532 ± 0.0041; n = 0.9286 ± 0.0364	0.068	1.684	0.9987	1.246	1.428	0.353	2.286

The Fritz–Schlunder V model achieved R^2 = 0.9987, demonstrating close numerical agreement with the experimental data. Its relatively low χ^2, ERRSQ, RMSE and ARE values also indicated acceptable fitting accuracy. However, the predicted capacity of 145.2860 mg g^{-1} was inconsistent with the measured adsorption range and the Langmuir capacity of 144.8515 mg g^{-1}. The model therefore offered a strong mathematical fit but a weak physical representation. Moreover, its five adjustable parameters increase the possibility of overfitting.

Comparison of all isotherms indicated that the higher-parameter equations improved R^2 without consistently reducing every error measure. The Freundlich model provided a simpler and physically reasonable description, with $1/n$ = 0.3551 and comparatively low errors. Accordingly, Rhodamine B uptake was predominantly associated with favourable adsorption on heterogeneous sites, although Langmuir-type occupation may also contribute. This interpretation should not be treated as proof of an exclusively multilayer mechanism. As reported in previous studies, magnetic AC@Fe_3O_4 nanocomposite prepared from pomegranate peel-derived activated carbon was developed for the adsorption of Pb(II), Cd(II), Cu(II), and As(III) ions. The adsorbent followed the Freundlich isotherm and pseudo-first-order kinetics, exhibiting spontaneous and endothermic adsorption with promising heavy metal removal efficiency (Ali *et al.* 2025).

3.13 Proposed Adsorption Mechanism

The interaction of Rhodamine B with the MnO_2/biochar nanocomposite was interpreted by combining the FTIR, BET, FESEM, UV–Vis, and PXRD observations with the kinetic and equilibrium results. The available evidence suggests that dye uptake may involve hydrogen bonding, electrostatic attraction, diffusion-driven pore filling, and π–π interactions.

Rhodamine B uptake may proceed through pore filling, hydrogen bonding, π–π stacking, and electrostatic attraction. Nitrogen adsorption–desorption analysis revealed a high surface area and accessible pores capable of accommodating dye molecules. The FESEM micrographs further confirmed a rough, porous morphology that provides numerous adsorption sites and facilitates diffusion into the internal structure. The mesoporous characteristics identified by BET analysis therefore support pore-filling as an important removal pathway.

The aromatic carbon domains indicated by UV–Vis and PXRD analyses may promote π–π interactions with the conjugated rings of Rhodamine B. PXRD additionally showed disordered carbon regions and MnO_2-related crystalline phases, although diffraction evidence alone cannot confirm hydrogen bonding. FTIR identified hydroxyl, carbonyl, C–O, and aromatic groups capable of participating in hydrogen bonding and surface interactions. Depending on solution pH and surface charge, the MnO_2/biochar interface may also attract cationic dye species electrostatically.

The kinetic and equilibrium analyses supported adsorption on chemically and energetically nonuniform sites. PSO produced the lowest overall kinetic errors, whereas Freundlich and several hybrid isotherms represented the equilibrium data effectively. These results indicate that Rhodamine B removal was governed by several concurrent interactions rather than a single adsorption pathway. However, PSO fitting alone does not conclusively establish chemisorption, and the electrostatic contribution should be confirmed using point-of-zero-charge and pH-dependent adsorption measurements.

3.14 Evaluation Using Real Water Matrices

The practical performance of the MnO_2/biochar nanocomposite for Rhodamine B removal was examined using tap, sewage, distilled, and industrial water. Turbidity, pH, electrical conductivity (EC), and TDS were measured before and after treatment, as summarized in Table 20.

Table 20. Physicochemical properties of industrial water before and after treatment

Entry	Parameter	Untreated Water	Treated Water	Reference Range
1	EC (µS cm^{-1})	1528 ± 5.16	1186 ± 6.42	900–1400
2	Turbidity (NTU)	4.38 ± 0.072	1.16 ± 0.028	0.5–5.0
3	pH	7.48 ± 0.018	7.12 ± 0.026	6.5–8.5
4	TDS (mg L^{-1})	764 ± 2.58	593 ± 1.46	≤1500

Each water sample was filtered through a 0.45-µm membrane and fortified with 75 mg L^{-1} Rhodamine B, corresponding to the highest concentration investigated in the Taguchi design. Adsorption experiments were subsequently performed under the selected operating conditions. The MnO_2/biochar nanocomposite reduced the dye concentration across the tested matrices, as presented in Fig. 18. Differences among the samples may be attributed to competing ions, dissolved organic matter and variations in water chemistry.

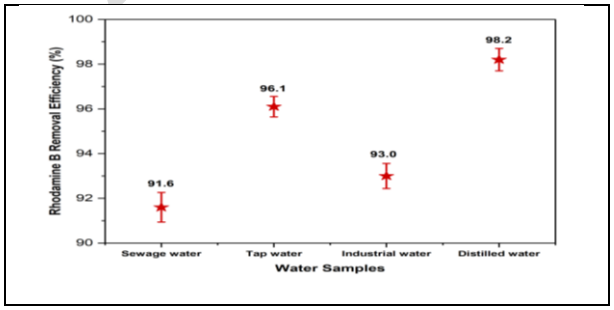

Fig. 18: Performance of the MnO_2/biochar nanocomposite in different water matrices

Figure 18 indicates that Rhodamine B removal from sewage and industrial water reached 91.6% and 93.0%, respectively. Their comparatively lower efficiencies may arise from dissolved ions, including Na^+, Mg^{2+} and Ca^{2+}, and natural organic matter competing with dye molecules for available adsorption sites. These constituents can obstruct accessible pores, occupy surface functional groups, and screen electrostatic interactions. Higher removal in tap and distilled water may be associated with their lower concentrations of competing species, allowing Rhodamine B to interact more readily with the composite surface and diffuse into its pores. Matrix interference was therefore more pronounced in industrial water and sewage.

3.15 Reusability

Regeneration performance of the MnO_2/biochar nanocomposite was investigated to assess its operational durability and potential treatment cost. Four consecutive adsorption–desorption cycles were conducted under selected conditions. After each adsorption experiment, the retained Rhodamine B was desorbed using 0.1 M NaOH, after which the recovered material was washed to neutral pH, dried, and reused. As illustrated in Fig. 19, removal efficiency gradually declined with increasing cycle number, possibly because of incomplete dye desorption, blockage of active sites, and minor material loss during recovery.

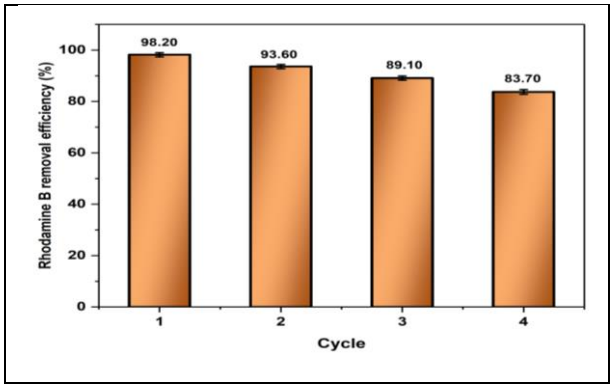

Fig. 19: Reusability of the MnO_2/biochar nanocomposite during four consecutive Rhodamine B adsorption–desorption cycles

Figure 19 presents the Rhodamine B removal efficiency over four consecutive regeneration cycles. Gradual performance loss may result from incomplete desorption, persistent dye retention, and progressive blockage of accessible adsorption sites. The limited release of Rhodamine B during NaOH treatment indicates that alkaline regeneration could not fully restore the original surface. Minor adsorbent loss and structural alteration during repeated washing may also contribute to the decline. In previous studies, Cu-doped MnO_2/rice husk carbon (3D-Cu-MnO_2@RHC) monolithic catalyst

was developed for peroxymonosulfate-activated dye degradation. The catalyst achieved 99.7% Rhodamine B degradation within 60 min and maintained over 99% efficiency for 10 consecutive cycles, demonstrating excellent stability and scalability for wastewater treatment (Zhou *et al.* 2026).

3.16 Management and Potential Reuse of the Spent Adsorbent

Following Rhodamine B adsorption, the exhausted MnO_2/biochar nanocomposite requires controlled management to prevent secondary contamination. Chemical regeneration can recover adsorption sites, extend material service life, and reduce the demand for fresh adsorbent. When regeneration is ineffective, thermal treatment may destroy retained dye molecules and permit partial recovery of the carbonaceous material; however, gaseous emissions must be appropriately controlled. Another possible route is immobilizing the spent nanocomposite within cement-based products, where the solid matrix may restrict contaminant release. Before either disposal or reuse, leaching tests should verify the stability of manganese and retained dye. These strategies provide potential pathways for safer handling and resource recovery, although their environmental and economic feasibility requires further assessment.

4. CONCLUSION

An MnO_2/biochar nanocomposite derived from pomegranate peel was successfully prepared and evaluated for Rhodamine B adsorption. FTIR, PXRD, FESEM, UV–Vis, and BET analyses confirmed the integration of MnO_2 with the carbonaceous matrix and demonstrated a porous adsorbent structure. The nanocomposite exhibited a BET surface area of 412.834 $m^2\ g^{-1}$, a total pore volume of 0.289 $cm^3\ g^{-1}$, and a mean pore diameter of 2.81 nm. Taguchi analysis identified 60 min contact time, pH 10, 0.05 g adsorbent dosage, and 75 mg L^{-1} initial Rhodamine B concentration as the preferred factor-level combination. ANOVA showed that adsorbent dosage and initial concentration contributed 56.26% and 37.50%, respectively, to adsorption capacity, whereas contact time and solution pH contributed 40.37% and 29.44% to removal-efficiency variation. MEREC assigned weights of 0.1071 and 0.8929 to removal efficiency and adsorption capacity, respectively, and MABAC selected Run 24 as the best experimentally tested compromise, producing 74.50% removal and an adsorption capacity of 85.53 mg g^{-1} at 60 min, pH 7, 0.05 g dosage, and 75 mg L^{-1} concentration. The confirmation errors for the optimized conditions were ≤0.23%, demonstrating close agreement between the predicted and experimental responses.

The engineered ANN–GA models produced cross-validated R^2 values of 0.8488 and 0.9173 for removal efficiency and adsorption capacity, respectively. However, quadratic regression achieved higher leave-one-out R^2 values of 0.9265 and 0.9777, indicating better predictive generalization for the limited L27 dataset. Among the kinetic models, the pseudo-second-order model provided the strongest overall fit with $R^2 = 0.9973$ and an estimated equilibrium adsorption capacity of 130.410 mg g^{-1}. The Langmuir model exhibited a high two-parameter isotherm fit with $R^2 = 0.9981$ and a maximum adsorption capacity of 144.8515 mg g^{-1}, while the overall equilibrium analysis indicated that adsorption occurred across chemically and energetically nonuniform surface sites through concurrent pore filling, hydrogen bonding, electrostatic attraction and π–π interactions. The nanocomposite also retained Rhodamine B removal capability in real water matrices and was reusable for four adsorption–desorption cycles, although gradual performance loss occurred because of incomplete desorption, active-site blockage and possible material loss. Overall, the developed MnO_2/biochar nanocomposite demonstrates promising laboratory-scale potential for dye removal; however, larger independent datasets, improved regeneration studies, manganese-leaching assessment, continuous-flow validation, scale-up and economic analysis are required before practical wastewater-treatment application.

FUNDING

This research received no specific grant from any funding agency in the public, commercial, or not-for-profit sectors.

CONFLICTS OF INTEREST

The authors declare that there is no conflict of interest.

REFERENCES

Akmese, B., Removal of Brilliant Blue R and Victoria Blue R dyes from textile wastewater by adsorption method using pomegranate peel, *BMC Chem.*, 19(1), 99(2025). https://doi.org/10.1186/s13065-025-01476-4

Ali, H. A. F., Samadi, M. A. and Turki, K. M., Synthesis and Characterization of AC@Fe_3O_4 Nanocomposite

and its Application as an Efficient Adsorbent for Removal of Some Heavy Metal Ions from Aqueous Solutions, *Iran. J. Chem. Chem. Eng.*, 44(9), 2234–2246 (2025). https://doi.org/10.30492/ijcce.2025.2055552.7036

Alorabi, A. Q., Sustainable Synthesis of PPHC@TiO_2/PPy Composite for Enhanced Congo Red Dye Removal: Kinetics, Isotherms, and Mechanistic Insights, *J. Clust. Sci.*, 36(5), 169(2025). https://doi.org/10.1007/s10876-025-02898-9

Aslam, A., Nadeem, N., Jilani, A., Al-Zaqri, N., Noreen, S., Zahid, M. and AlObaid, A. A., Visible Light Driven MnO_2/MnS Hybrid Nanostructures for Photocatalytic Degradation of Organic Pollutants: A Synergistic Approach for Wastewater Treatment, *Chem. Select*, 10(34), e03184 (2025). https://doi.org/10.1002/slct.202503184

Assefa, H. and Subramaniam, S. K., Mechanistic and Kinetic Evaluation of Hexavalent Chromium Adsorption Using Polyaniline-Functionalized $Ti_3C_2T_x$ MXene Composite, *Nanomater. Nanotechnol.*, 2025(1), 7391984(2025). https://doi.org/10.1155/nax2/7391984

Aziam, R., Stefan, D. S., Nouaa, S., Ungureanu, C., Chiban, M. and Stefan, M. T., Mechanism of Competitive Adsorption of Phosphate and Nitrate by Ternary Biopolymer–Bentonite Beads, *Environ.*, 13(6), 340(2026). https://doi.org/10.3390/environments13060340

Azizi, M. and Alorabi, A. Q., One-pot synthesis of kaolinite–modified pomegranate hydrochar composite for enhanced malachite green removal, *J. Environ. Chem. Eng.*, 13(6), 119379(2025). https://doi.org/10.1016/j.jece.2025.119379

Benahdach, K., Aoulad El Hadj Ali, Y., Azzouz, A., Mar Cerrillo González, M. D., Chraka, A., Mail, R. E., Laghdach, A. E., Wahby, A. and Arhoun, B., Synthesis of activated carbon by microwave-assisted sulfuric acid activation for the adsorption of Congo Red in aqueous medium: Kinetic, isotherm, thermodynamic, molecular dynamic, and functional theory studies, *J. Mol. Liq.*, 420, 126821(2025). https://doi.org/10.1016/j.molliq.2024.126821

Beriber, A., Berrama, T., Doufene, N., Zekkaoui, C. and Dadou, S., Use of desalination plant brine activated bamboo stalks as a novel biosorbent to dyestuff removal, *Biomass Convers. Biorefine.*, 14(15), 17423–17442 (2024). https://doi.org/10.1007/s13399-023-04183-z

Cao, M., Zhuang, Z., Liu, Y., Zhang, Z., Xuan, J., Zhang, Q. and Wang, W., Peptide-mediated green synthesis of the MnO2@ZIF-8 core–shell nanoparticles for efficient removal of pollutant dyes from wastewater via a synergistic process, *J. Colloid Interf. Sci.*, 608, 2779–2790 (2022). https://doi.org/10.1016/j.jcis.2021.11.003

Cardoso, N. F., Lima, E. C., Pinto, I. S., Amavisca, C. V, Royer, B., Pinto, R. B., Alencar, W. S. and Pereira, S. F. P., Application of cupuassu shell as biosorbent for the removal of textile dyes from aqueous solution, *J. Environ. Manage.*, 92(4), 1237–1247 (2011). https://doi.org/10.1016/j.jenvman.2010.12.010

Chaabane, L., Beyou, E. and Baouab, M. H. V., Preparation of a novel zwitterionic graphene oxide-based adsorbent to remove of heavy metal ions from water: Modeling and comparative studies, *Adv. Powder Technol.*, 32(7), 2502–2516(2021). https://doi.org/10.1016/j.apt.2021.05.011

Chen, P., Cheng, Z., Zhang, X., Zhang, L., Zhang, X., Tang, J. and Qiu, F., Efficient degradation of dye wastewater by catalytic ozonation reactive ceramic membrane with facile spraying of nano Ti[sbnd]Mn oxides: A pilot scale attempt, *J. Water Process Eng.*, 55, 104143(2023). https://doi.org/10.1016/j.jwpe.2023.104143

Deepha, R. and Senthilnathan, V., A sol-gel Technique Was Used to Synthesize Ce-doped TiO_2 Nanoparticles, Which Were Then Used as Photocatalysts to Degrade Rhodamine B (RhB) and Eosin Y (EY) Dyes Under UV Light, *J. Environ. Nanotechnol.*, 15(2), 605–615 (2026). https://doi.org/10.13074/jent.2026.06.2622248

Derkaoui, K., Bencherifa, I., Mebdoua, Y., Boukhouidem, K., Hadjersi, T., Chetoui, A., Naama, S., Friha, S., Kechouane, M. and Kaci, M. M., Novel SiNWs/MnO_2/$Ni(OH)_2$ Heterostructure as Photocatalyst for Efficient Degradation of Rhb Under Visible Light, *J. Inorg. Organomet. Polym. Mater.*, 35(5), 4144–4161 (2025). https://doi.org/10.1007/s10904-024-03517-2

El-Mahdy, N. A., El-Gharkawy, E.-S. R. and Akl, M. A., Novel delafossite structured visible-light sensitive $AgFeO_2$/PPAC nanocomposite for efficient adsorptive photocatalytic degradation of cationic and anionic dyes, *Sci. Rep.*, 16(1), 21420(2026). https://doi.org/10.1038/s41598-026-60824-z

Elnjikkal, J. R. and Dwivedi, M., Microwave vacuum drying of pomegranate peel: Evaluation of specific energy consumption and quality attributes by response surface methodology and artificial neural network, *J. Food Proce. Preser.*, 46(3), (2022). https://doi.org/10.1111/jfpp.16325

Erian, G. R., Abdelmonem, N., Abdelghany, A., Abou-Shady, H. and Rahman, R. O. A., Microstructure-guided design of biopolymer-supported tri-phasic TiO_2 for sustainable lead and cadmium detoxification, *Sci. Rep.*, 16(1), 10530(2026). https://doi.org/10.1038/s41598-026-43155-x

Fadhil, D. H., Al-Mashhadani, M. H., Mortada, W. I., Alsayed, R. and Khalifa, M. E., Eco-derived chitosan–cellulose hybrid from pomegranate peel for enhanced uptake of methyl orange dye, *Res. Chem.*, 27, 103371(2026). https://doi.org/10.1016/j.rechem.2026.103371

Ganvir, V. Y., Alvi, S. N. A., Musrif, P. G., Vadivel, M., Kumar, P. S. and Ulloa, N., Sustainable Mechanochemical Fabrication of $NiFe_2O_4$@rGO Conductive Hybrid for Energy Storage and

Environmental Remediation, *J. Environ. Nanotechnol.*, 15(1), 478–491(2026). https://doi.org/10.13074/jent.2026.03.2541991

Hamed, M. M., Ali, M. M. S. and Aglan, R. F., Thermal Decomposition Route for Synthesis of Pure-Phase Zirconium Dioxide Nanocrystals and their Application in the Sorption of Molybdenum Ions in Nitric Acid Solution, *Water, Air Soil Pollut.*, 237(11), 661 (2026). https://doi.org/10.1007/s11270-026-09246-1

Hamrouche, N., Djilani, C., Belhocine, Y., Bouzenad, N., Amir, L. B., Meradi, S., Hamrouche, I. and Ben, A. D. S., Comprehensive characterization and RSM-based optimization of crystal violet adsorption using $SnCl_2$–$FeCl_3$and $SnCl_2$–$ZnCl_2$ activated pomegranate peel biosorbents, *RSC Adv.*, 16(5), 4318–4334 (2026). https://doi.org/10.1039/d5ra09290f

Hamrouche, N., Djilani, C., Magri, P., Belhocine, Y., Djazi, F., Kezzar, M. and Bouzenad, N., A novel biosorbent from raw pomegranate peel modified with $SnCl_2$/$FeCl_2$ for the adsorption of crystal violet cationic dye: response surface methodology process optimization, thermodynamic, kinetic, isotherm, and recyclability studies, *Biomass Convers. Biorefine.*, 15(6), 9445–9461 (2025). https://doi.org/10.1007/s13399-024-05737-5

Hassan, M. A., El-Ashaal, E. S., Oun, A. A. and Farghali, M. A., Pomegranate Peel/Reduced Graphene Oxide-Based Nanocomposite as a Promising Adsorbent for Lead and Methylene Blue Remediation, *Chem. Africa*, 8(9), 4693–4715 (2025). https://doi.org/10.1007/s42250-025-01406-w

He, R., Hou, X., Wang, F. and Liu, X., Fabrication of α-MnO_2/GO/PVDF Catalytic Membranes via a Phase Inversion Method for Universal Separation and Degradation of Dye Wastewater, *ACS Omega*, 11(5), 8773–8783 (2026). https://doi.org/10.1021/acsomega.5c12589

Kamalesh, R. and Saravanan, A., Sustainable ANN-driven modelling and characterisation of Rhodamine-B removal using ZIF-8 functionalised pomegranate peel waste adsorbent supporting clean water and sanitation initiatives, *Hybrid Adv.*, 12, 100625(2026). https://doi.org/10.1016/j.hybadv.2026.100625

Kandasamy, N., Shanmugam, P., Parasuraman, B., Periyasami, G., Boonyuen, S., Thangavelu, P., Palanisamy, K. L. and Thangarasu, P., Boosting photodegradation performance through efficient MnO_2/rGO nanocomposite: water remediation application, *J. Sol-Gel Sci. Technol.*, 117(3), 68(2026). https://doi.org/10.1007/s10971-025-07093-w

Khedr, M., Waly, A. I., Hafez, A. I., Ali, H. M., Gadallah, H. and Sabry, R., Integrated economic and adsorption performance study of CMC/MMT nano-composite for cationic dye removal from industrial wastewater, *Sci. Rep.*, 16(1), 7726(2026). https://doi.org/10.1038/s41598-026-36615-x

Kreetachat, T., Kandasamy, B., Govindasamy, P., Phibanchon, S., Nakyai, T., Pannaracha, P., Pahasup-anan, T., Chotigawin, R., Wongcharee, S. and Suwannahong, K., MWCNT/Ag/β-MnO_2 Hybrid Nanostructures for Optimized Photocatalytic Wastewater Treatment via Unified Kinetic Modeling, *Res. Eng.*, 29, 108890(2026). https://doi.org/10.1016/j.rineng.2025.108890

Kumar, A., Poornima, S. N., Subbulakshmi, R., Selvaraju, M., G, R. K. and Jayabalan, C., Hierarchical green carbon fibers from banana pseudostem for efficient Pb^{2+} adsorption: Kinetics, isotherms, and machine learning prediction, *Interact.*, 247(1), 188(2026). https://doi.org/10.1007/s10751-026-02534-6

Li, Z., Guan, T., Shi, H., Wang, C., Peng, X. and Wang, S., Facile Synthesis of MnO_2 Catalysts on 3D Nickel Foam for Efficient Degradation of Rhodamine B by Activating Peroxymonosulfate, *Catal. Lett.*, 156(2), 38(2026). https://doi.org/10.1007/s10562-025-05275-3

Loganathan, A., Sethupathi, N., Mahalingam, P. and Sivakumar, P., Green Synthesis, Structural Characterization and Kinetics of Photocatalytic Degradation of Reactive Blue 19 Dye Using CeO_2-doped Reduced Graphene Oxide Nanohybrid, *J. Environ. Nanotechnol.*, 15(1), 576–585 (2026). https://doi.org/10.13074/jent.2026.03.2612126

Mahdy, A. and Fathi, N., Comparative Performance of Bio-Derived Nanomaterials for Chromium Removal from Contaminated Water, *Water Environ. Res.*, 98(4), e70382(2026). https://doi.org/10.1002/wer.70382

More, P. R. and Arya, S. S., Intensification of bio-actives extraction from pomegranate peel via microwave irradiation: Effect of factors, optimization, kinetics, and bioactive profiling, *Chem. Eng. Proce. Process Intensifi.*, 202, 109839(2024). https://doi.org/10.1016/j.cep.2024.109839

Murat, D., Teğin, İ. and Saka, C., Optimization of nitrogen doping via microwave irradiation for improved adsorptive performance of pomegranate peel-derived biochar, *Chem. Eng. Res. Des.*, 220, 566–576 (2025). https://doi.org/10.1016/j.cherd.2025.07.040

Nayab, M., Farhan, A., Zahid, M., Rehan, Z. A., Jilani, A., Almeer, R., Ibrahim, H. and Al-Zaqri, N., Solar-Driven Photocatalytic Degradation of Organic Pollutants by I-MnO_2/PTh Nanocomposite: Mechanisms, Kinetics, and Implications for Advanced Environmental Remediation, *Int. J. Environ. Res.*, 20(1), 48(2026). https://doi.org/10.1007/s41742-025-01012-1

Nouacer, I., Hammadi, S., Benalia, M., Djedid, M. and Bencheikh, S. E., Biosorption of carcinogenic metal ions using the immobilized microalgae Auxenochlorella protothecoides on a lignocellulosic matrix: Optimization, kinetic, isotherm and

mechanism, *South Afr. J. Bot.*, 157, 297–313 (2023). https://doi.org/10.1016/j.sajb.2023.02.023

Rao, D. P., Krishnasamy, V. D., Selvaraju, M., Sundramurthy, V. P., Kandavalli, S. R., Chitra, M. S., Sivasamy, N. and Thirumoorthy, P., Adsorptive removal of cadmium from electroplating wastewater using hybrid composite of thiol-grafted seed gum of Tamarindus indica and Teff hay biocarbon, *Zeitschrift Fur Physikalische Chemie*, 239(5), 633–654 (2025). https://doi.org/10.1515/zpch-2024-0715

Romero, G. D., Crocce, R. E. D., Soares, T. J. A. and dos Passos, G. B. M., Biosorption Isotherms and Thermodynamic Insights into Metal Recovery from Li-Ion Battery Leachates Using Fungal Biomass, *ACS Sustain. Chem. Eng.*, 14(14), 6668–6680(2026). https://doi.org/10.1021/acssuschemeng.5c13174

Saad, H., Turki, T., Srasra, M. and Srasra, E., Sorption behavior of pomegranate polyphenols on surfactant-modified clays in aqueous solution, *Sci. Afr.*, 27, e02568 (2025). https://doi.org/10.1016/j.sciaf.2025.e02568

Shirali, A., Ebrahimi, M., Hemmati-Sarapardeh, A., Ranjbar, M. and Schaffie, M., Comparative analysis of natural and synthetic surfactant adsorption by quartz minerals: an experimental study, *Sci.,* 16(1), 7852 (2026). https://doi.org/10.1038/s41598-026-39608-y

Sihag, S. and Pal, J., Adsorption of fluoride ions from aqueous solution by rice husk based nanocellulose, *Adv. Environ. Technol.*, 9(3), 194–214 (2023). https://doi.org/10.22104/aet.2023.5963.1643

Simonetti, G., Di Filippo, P., Pomata, D., Riccardi, C., Buiarelli, F., Parisi, S., Petrangeli, P. M., Senofonte, M. and Lorini, L., Pinewood Biochar as an Affordable Adsorbent for Short- and Medium-Chain PFAS Removal from Contaminated Water, *Mol.*, 31(7), 1100(2026). https://doi.org/10.3390/molecules31071100

Sugumar, M., Bharathi, S., Sampath, V., Sundramurthy, V. P., Selvaraju, M., Kadaikunnan, S. and Khaled, J. M., Biosorption of Pb(II) ions through nanostructured teff straw based magnetized activated biocarbon: Aspects on modeling, optimization, and kinetics, *Global Nest J.*, 26(9), 06479(2024). https://doi.org/10.30955/GNJ.06479

Sumathi, A., Kamatchi, T., Maruthavanan, T. and Epshiba, R., Green synthesis of SnO_2–TiO_2 nanocomposite using pomegranate peel extract for efficient photocatalytic degradation of Alizarin Red dye, *Chem. Pap.*, (2026). https://doi.org/10.1007/s11696-026-05144-2

Yahuza, S., Manogaran, M., Yasid, N. A., Othman, A. R. and Shukor, M. Y. A., Equilibrium, kinetics, and thermodynamic studies on the biosorption of Reactive Red 120 dye utilizing the biomass of Enterobacter sp. MMO5, *Asia-Pac. J. Mol. Bio. Biotechnol.*, 32(4), 135–163 (2024). https://doi.org/10.35118/apjmbb.2024.032.4(Special).11

Zhou, Z., Jiang, B., Li, X., Xu, R., Li, J., Bian, J., Li, C. and Zhan, G., Multi-Level Engineered 3D-Printed Monolithic Catalyst with Dual-Defect Synergy for Enhanced Advanced Wastewater Treatment, *Chem. Eng. Sci.*, 334, 124329(2026). https://doi.org/10.1016/j.ces.2026.124329